

**MODELING OF THERMAL STORAGE SILOS AND HEAT EXCHANGER
FOR PARTICLE-BASED CONCENTRATED SOLAR POWER**

A Thesis
Presented to
The Academic Faculty

By

Matthew Alexander Marton

In

In Partial Fulfillment
of the Requirements for the Degree in
Master of Science in the
School of Mechanical Engineering

Georgia Institute of Technology

August, 2024

COPYRIGHT © 2024 BY MATTHEW MARTON

MODELING OF THERMAL STORAGE SILOS AND HEAT EXCHANGER FOR PARTICLE-BASED CONCENTRATED SOLAR POWER

Approved by:

Dr. Comas Haynes, Co-Advisor
Aerospace, Transportation, and Advanced
Systems
Georgia Tech Research Institute

Dr. Shannon Yee
School of Mechanical Engineering
Georgia Institute of Technology

Dr. Peter Loutzenhiser, Co-Advisor
School of Mechanical Engineering
Georgia Institute of Technology

Dr. Juan Ordóñez
College of Engineering
*Florida A&M University-Florida State
University*

Date Approved: July 24, 2024

For my grandmother, I hope this makes you proud

ACKNOWLEDGEMENTS

Throughout the two years I have spent working on this thesis I have been supported by an amazing group of people. First and foremost, I have to thank my advisor Dr. Comas Haynes who has given me all these opportunities. I was days away from having to turn down my offer to come to Georgia Tech due to lack of funding when you offered me the opportunity to work on this project. I will never be able to repay that. To my co-advisor, Dr. Peter Loutzenhiser, thank you for taking me into your group on the word of Dr. Haynes. I learned more about CSP and solar fuels than I could have ever expected upon entering the university. Hearing Professor Steinfeld speak at the ASME conference in 2024 made me fully understand your passion for this work. My only regret is that we did not get to work together more. Next there is Dr. Juan Ordóñez and Juan Camillo at FAMU-FSU who have been on this journey with me. You guys were effectively another lab group for me and the hours spent in meetings and presentations bouncing ideas off of each other absolutely made this thesis possible. Last, but certainly the most important, my friends and family who have supported me. Thank you, Megan, Carli, David, and Caroline, for spending countless hours of the last two years listening to me complain about the process of MATLAB development. If Louisiana Tech gave me nothing else, it gave me the best friends in this world. To my mom, dad, and brother, I love you guys tremendously. All I can do is wake up everyday and try to make you guys proud.

TABLE OF CONTENTS

ACKNOWLEDGEMENTS	iv
LIST OF TABLES.....	vi
LIST OF FIGURES	vii
LIST OF SYMBOLS AND ABBREVIATIONS	ix
SUMMARY	xi
CHAPTER 1: INTRODUCTION	1
CHAPTER 2: SUBCOMPONENT MODEL DESCRIPTION	7
2.1 Heat Exchanger	8
2.2 Particle Storage Silo	17
CHAPTER 3: COMBINED SYSTEM MODEL AND EXERGY ANALYSIS	29
3.1 Combined Heat Exchanger and Storage Silo	29
3.2 Exergy Analysis.....	37
CHAPTER 4: CONCLUSION	48
REFERENCES	52

LIST OF TABLES

Table 1: Geometric and Physical Properties of Heat Exchanger	10
Table 2: Boundary Conditions and Flow Physical Properties for Initial Heat Exchanger Test	11
Table 3: Particle, sCO ₂ and Wall Temperatures 25 Minutes	14
Table 4: Sensitivity Analysis Results of Heat Exchanger	14
Table 5: Geometric Dimensions of Stored Particles	19
Table 6: Insulation Properties	19
Table 7: Base Case for Storage Silo Sensitivity Analysis.....	26
Table 8: Results of Storage Silo Sensitivity Analysis	27
Table 9: Base Case for Combined System Modeling	31
Table 10: Exergetic Efficiency Analysis for Heat Exchanger Based on Lower Sensitivity Analysis from Table 4	39
Table 11: Fard et al. Exergetic Efficiency vs Calculated Value [22-24]	40
Table 12: LMTD for Cases Shown in Table 10 vs LMTD for Fard et al. Data	41
Table 13: Entropy Generation Rate and Number for Modeled Heat Exchangers.....	42

LIST OF FIGURES

Figure 1: Gen 3 Particle Pilot Plant Concentrated Solar Power Plant [3]	1
Figure 2: CARBO Ceramic Particles Showing Oxidation Overtime from A-C [3]	2
Figure 3: Global Average Weighted Cost of Electricity in 2018 [5].....	3
Figure 4: Left: Heat Exchanger’s Position within CSP System.....	8
Figure 5: Diagram of a Particle-to-sCO ₂ Moving Packed-Bed Heat Exchanger. sCO ₂ in Blue and Particles in Red [9].....	9
Figure 6: Particle, sCO ₂ and Wall Temperatures 2.5 Minutes.....	12
Figure 7: Particle, sCO ₂ and Wall Temperatures 10 Minutes.....	12
Figure 8: Particle, sCO ₂ and Wall Temperatures 25 Minutes.....	13
Figure 9: Diagram of Silo and Heat Exchanger Relative to CSP System.....	17
Figure 10: Top: Vertical Cross Section of Storage Silo. Bottom: Horizontal Cross Section of Storage Silo. Black: CARBO HSP 40/70, Yellow: Brick Inner Liner, Blue: Insulmix 19L, Gray: Elmtherm 1000 MP.....	18
Figure 11: Temperature of Particles and Silo Insulation Over 10 Hours	21
Figure 12: RC Network of a Silo Insulation Layers	23
Figure 13: Temperatures of Stored Particles and Insulation Over 100 Hour in Quasi-Steady State	24
Figure 14: a) Top: Particle and Insulation Temperature after 10 Hours with Particle Velocity of 0.0033 m/s. b) Bottom: Velocity of 0.006 m/s	25
Figure 15: Diagram of Mass Flows in Combined Storage and Heat Exchanger System	30
Figure 16: Particle and Insulation Temperatures for Storage Silo Over 10 Hours	32
Figure 17: Heat Exchanger Outlet Temperatures for Combined System.....	33

Figure 18: Particle Flow Decreased to 0.01 kg/s, Inlet Temperature Drop to 375°C and Then Rise over 1.5 Hours, sCO ₂ Inlet Dropped by 200°C	34
Figure 19: Particle Flow Back to 0.02 kg/s, sCO ₂ Flow Decreased to 0.01335 kg/s, Same Temperature Change as Figure 18	35
Figure 20: Particle and Gas Flow Return to Base Case, Inlet Temperature Dropped to 250°C for 4.5 Hours, sCO ₂ Inlet Dropped by 200°C	36
Figure 21: Control Volume Boundary of Heat Exchanger for Exergy Analysis.....	39

LIST OF SYMBOLS AND ABBREVIATIONS

A	Area
α	Thermal Diffusivity
Bi	Biot Number
C_p	Heat Capacity
C	Heat Capacitance
E	Exergy
e_f	Flow Exergy
ε	Exergetic Efficiency
f	Darcy Friction Factor
h	Enthalpy
H	Height
\bar{h}	Heat Transfer Coefficient
k	Thermal Conductivity
KE	Kinetic Energy
L	Length
\dot{m}	Mass Flow Rate
Nu	Nusselt Number
N_s	Entropy Generation Number
P	Perimeter
Pe	Peclét Number
Pr	Prandtl Number
PE	Potential Energy
Q	Heat Transfer
R	Thermal Resistance
Re	Reynolds Number
ρ	Density
S	Entropy

sCO₂ Super Critical Carbon Dioxide
T Temperature
t Time
th Thickness
u Internal Energy
U Overall Heat Transfer Coefficient
 \vec{u} Flow Velocity
w Width

Subscripts:

b Bulk
CO₂ Super Critical Carbon Dioxide
p or s Particles
w Wall
0 Dead State
 ∞ Far Field

SUMMARY

Concentrated solar power utilizing high temperature particles as the heat transfer fluid, coupled with long term storage provides a useful new method for baseload power. To progress the development of this technology, there is the need for a real time transient model of a CSP plant for use in both the operation and development of CSP plants. This work helps lay the foundation for this through the creation of computationally simple models of a particle to supercritical carbon dioxide heat exchanger and a particle storage silo. The heat exchanger is one dimensional and based upon previously completed work. The particle storage silo is quasi-one dimensional where the stored particle bed is captured through one equation and then coupled to the silo walls through an RC network. These models provided accurate results compared to the more complex existing models. After the creation of the individual component models, they were combined together into one continuous subsystem in preparation for their eventual inclusion in a full system model. Finally, exergetic efficiency analysis was performed on the heat exchanger and the combined subsystem to get a full picture of the energy flows in the system. The creation of these models will allow the future creation of a full system level model, as well as, the creation of active control schemes for managing CSP plants.

CHAPTER 1: INTRODUCTION

As the world transitions to renewable energy, concentrated solar power (CSP) is attracting attention for use in regions with consistently high direct normal irradiation (DNI) like southern Spain and the southwest United States. CSP operates by using a series of mirrors to concentrate the incoming solar radiation on to a receiver containing a heat transfer medium. The two most common approaches are the solar trough and the solar tower [1]. In the solar trough, a tube is set at the focal point of a parabolic mirror, and the heat transfer fluid flows between mirrors. However, in a solar tower system, a field of heliostats surround a central receiver placed atop a tall tower. A key advantage presented by the solar tower system over the solar trough, are the increased operating temperatures of the solar tower. Trough-type systems are limited to 500°C, while solar towers can reach up to 2000°C [2]. If the energy can be properly harnessed, these higher temperatures allow a greater energy efficiency. Research into high temperature CSP applications has recently gathered a lot of attention, with projects like the Gen 3 Particle Pilot Plant at Sandia National Lab (Figure 1) scheduled to come online in 2024 [3].

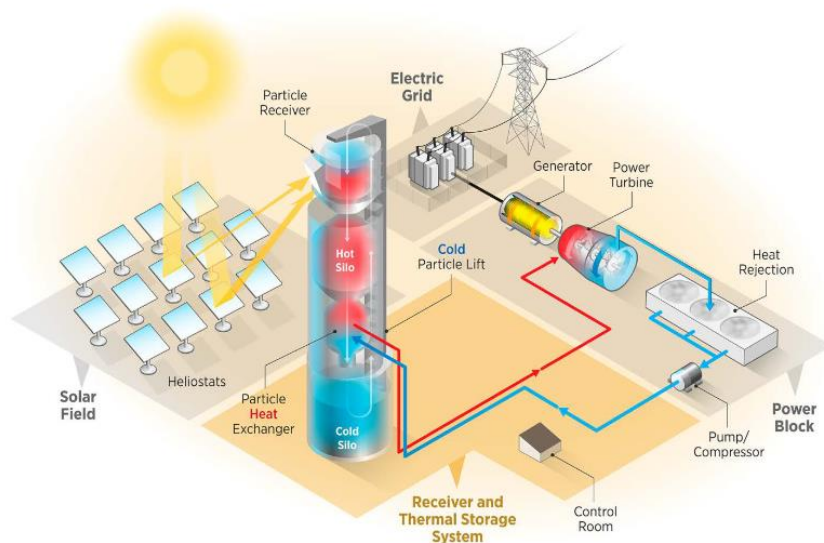


Figure 1: Gen 3 Particle Pilot Plant Concentrated Solar Power Plant [3]

To take advantage of the higher operating temperatures, the next generation of solar tower CSP projects are intended to use particles like CARBO HSP 40/70 sintered bauxite particles as the heat transfer material [4]. Conventional CSP plants use materials like oil, molten salts, or water for the heat transfer fluids. However, at the elevated temperatures that tower style plants can reach ($>1000^{\circ}\text{C}$) these materials can break down or are generally corrosive [1]. These sintered particles are very stable at high temperatures and demonstrate high solar absorption. Figure 2 shows these particles and the process of oxidation overtime. Even with the oxidation the particles still maintain their ideal properties.



Figure 2: CARBO Ceramic Particles Showing Oxidation Overtime from A-C [3]

These extreme temperatures allow the use of supercritical carbon dioxide (sCO_2) Brayton Cycles for power generation. sCO_2 Brayton Cycles are a proposed adaptation of the Brayton Cycle where the working fluid is sCO_2 in contrast to conventional air. On the high-pressure side, the cycle operates at over 7 MPa, which leads to an efficient conversion of input heat to output electrical power [5]. Implementing a sCO_2 cycle into a CSP plant would help bring the levelized cost of electricity [LCOE] down to a commercially competitive range. As Yin et al. explain,

replacing the steam-Rankine cycle in current generation CSP plants with a sCO₂ cycle, reduces the LCOE by 8% [5,6]. With CSP expected to naturally grow to at least 4% of total power generation globally by 2050, making the systems cheaper and more efficient are important problems to solve [7]. Figure 3 below details the costs of various power generation technologies in 2018 dollars. As shown, current generation CSP technologies are one of the most expensive methods to generate electricity. A CSP plant with a particle based thermal energy storage system and a sCO₂ power cycle could bring this cost down to viable levels.

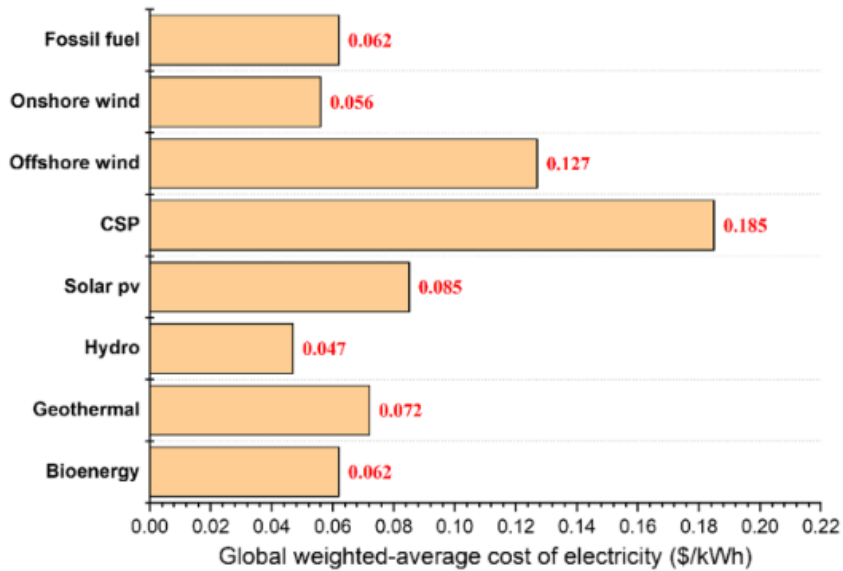


Figure 3: Global Average Weighted Cost of Electricity in 2018 [5]

A key step in advancing the next generation of CSP plants is the development of computational models. These models should take inputs like DNI and downstream power demand and predict the various component level responses in the power block, heat exchanger, storage system, receiver, and heliostat field. The connections between these subcomponents can be seen in Figure 1. The most powerful currently existing system level model is the System Advisor Model (SAM) developed at the National Renewable Energy Lab (NREL) [8]. SAM was developed as a general-purpose system model for technoeconomic analysis of renewable energy projects. While

SAM has a large amount of detail, the technoeconomic analysis portion is an unnecessary step for some portions of plant design. The models developed for this work were created for use in a simpler system level model focused on tracking thermal transients. Development of these models aids in the design and operation of CSP plants by allowing for plant operators to plan for changing stimuli. This work focuses on the creation of component models for the particle storage silos and the heat exchanger that transfers heat from the particles to the power block. These models should be computationally fast and accurate for inclusion in a later system level model being developed at Florida Agricultural and Mechanical University (W911SR-14-2-0001-W911SR22F0095 (62)). To further this goal, the heat exchanger and storage silo models were combined and their independent and combined reactions were tracked. There had been previous work in the field on developing these models, but they were often complex, leading to longer computational run times. Kevin Albrecht and Clifford Ho led efforts at Sandia National Lab to develop a model of a moving packed bed heat exchanger for particle-to-sCO₂ heat transfer [9]. Their initial efforts resulted in the creation of 2D heat exchanger model that tracked the temperatures of the particles, the sCO₂, and heat exchanger material. The work was eventually simplified to a 1D model where the flow properties were taken from the 2D model. Also at Sandia, Jeremy Sment led the development of models for the particle storage silos [10]. They used conventional computational fluid dynamics software like Fluent to model the heat transfer of storage silos. However, implementing an external solver into a system level model is problematic especially when the model is intended to be dynamic and responsive. At the same time the work presented here was being developed, Jeremy Sment and Kaden Plewe were developing their own model of a particle storage silo [11]. Similar to the initial efforts in heat exchanger modeling, Sment and Plewe's initial model is two dimensional. The model presented in this work, however, is a one-dimensional model. Sment and

Plewe's work provides a good baseline as a comparison against which to judge the computationally simpler model against. Moving beyond component models completion, a final goal was to complete sensitivity analyses of both the individual components and the combined model. Several variables were tested including the particle material properties, silo geometry, heat exchanger geometry, and fluid flow properties in the heat exchanger. The effect that changing these properties had on the final temperature outcomes could not be distinguished. This would further the goal of helping to design and operate future CSP plants.

The initial modeling work was completed in MATLAB due to the presence of a built in ordinary differential equation (ODE) solver [12]. A series of differential equations were input to the ODE solver, where the solver iteratively solved for the requested variables. To make the model reactive, an event handler was attached to the ODE solver. An event handler tracks the current solution of the solver and waits for an "event" to occur. These events could be a variable crossing a certain threshold or a set amount of time passing. When the event occurs, the handler either stops the program running fully, or pauses the program to inject new information into the solution. This was a required step because the ODE solver could only create continuous solutions. If, for example, the mass flow rate of heat storage media suddenly changed, this would create a discontinuity that would disengage the solution space. The event handler could be used to pause the solution, change the mass flow rate, and then restart the solver. MATLAB is also simple to use to combine the two separate silo and heat exchanger models together to create a connected subsystem. There are preexisting MATLAB frameworks as well for the creation of parametric studies. A future step in the full system model creation would be to move the model into the Modelon environment [13]. Modelon is a system modeling language that is built to handle large systems like CSP plants.

Modelon also has the advantage of being used by the CSP team at the National Renewable Energy Lab so that the models can be shared.

The final work presented here included component level models of a shell and plate, moving packed bed, particle-to-sCO₂ heat exchanger; a hot and cold particle storage silo; and a combined silo-heat exchanger model. Then, both individually and combined, the models were subjected to a parametric study covering a range of design variables. After the completion of this study, the models were transitioned to partners at FAMU for integration into the full CSP system level model.

CHAPTER 2: SUBCOMPONENT MODEL DESCRIPTION

Previous work in this space has focused on the development of complex multi-dimensional models; however, there is a need for simpler component models. Simpler component models can then be combined into a full system level model that can run in real time for both the operation and development of CSP plants. The components developed here serve as the building blocks for future work on system level modeling and control. These components have seen various levels of model development in the past. Mentioned previously, Albrecht and Ho created an initial model of the particle based moving packed-bed shell-and-plate heat exchanger being created for the G3P3 project [9]. This model focused on tracking the inlet and outlet temperatures of the flowing particles and the working fluid, as well as the heat exchanger material. During the system start up sequence, and during normal operation, the heat exchanger can experience temperature swings of several hundred degrees Celcius, therefore tracking the structure temperatures helps predict potential failure points due to thermal stresses. At the system level, the effects of the particle and working fluid flow rates on the heat exchanger can be tracked as well.

Attached to the heat exchanger are two storage silos for the hot and cold particles. Previous work on particle storage silos has been accomplished through either commercially available CFD software or a heat kernel method [10,11]. However, the model presented here captures the heat transfer from the particles in a quasi-one-dimensional framework similar to the modeling of fins. Due to the heavy amount of insulation on the storage silos, conduction through the particles is the primary mode of heat transfer and this is coupled to the insulation layers using an overall heat transfer coefficient. The silo design presented here is intended to store the particles for 10 hours and release them over an 8-hour cycle. A distinct addition to the model compared to other models is the usage of the Zehner, Bauer, and Schlunder (ZBS) model for calculation of the heat

conduction coefficient in the packed particle bed [14,15]. The ZBS model incorporates interparticle radiation to generate an accurate picture of heat conduction. For utilization within the numerical model, the solution for the ZBS conduction is linearized.

The following two subsections further detail the models developed for the heat exchanger and storage silos. First, the model originally created by Albrecht and Ho will be examined in further detail and the model verification steps are explored. Following the heat exchanger, the process of creating the quasi-1D storage silo model is discussed.

2.1 Heat Exchanger

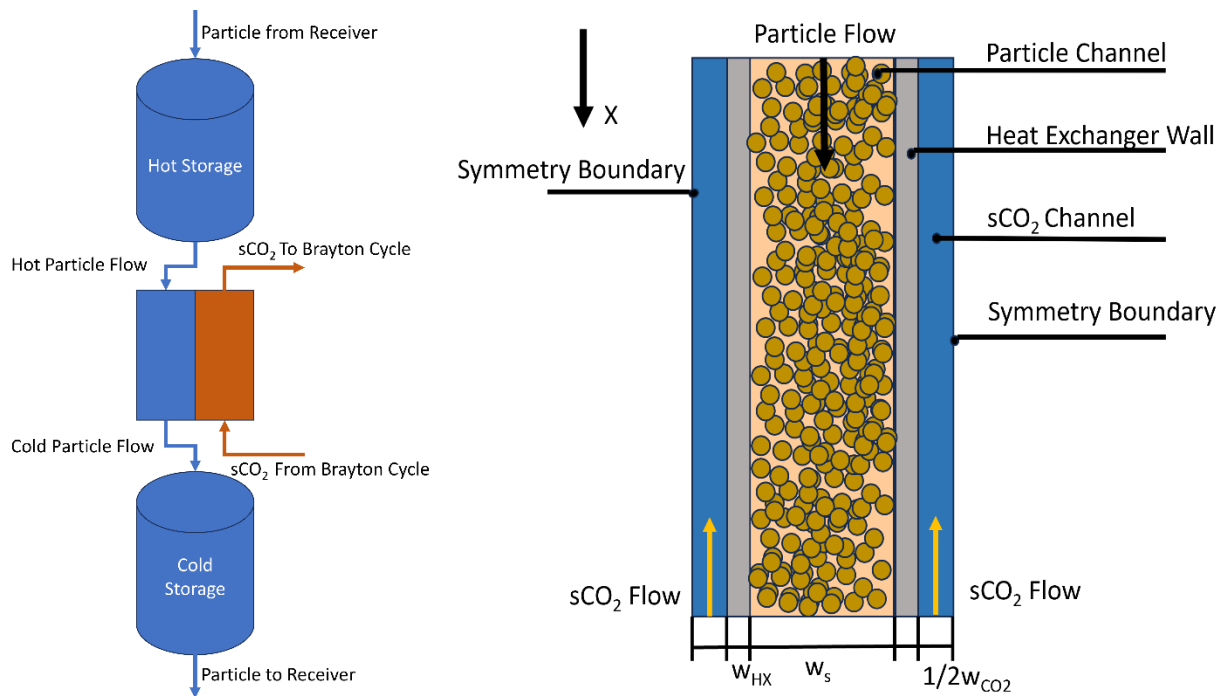


Figure 4: Left: Heat Exchanger's Position within CSP System

Fernández-Torrijos expanded on the work previously done by Albrecht and Ho to test the model more extensively [16]. Where Albrecht and Ho's work focused primarily on the creation of a 2D model for the heat exchanger, Fernández-Torrijos simplified the model to one dimension. Given their goal of tracking the outlet temperatures primarily, and a thin separating wall segment,

the added dimension was deemed unnecessary. The other advantage of using this one-dimensional approach is the computational speed when compared to a full 2D model. With the eventual goal of using this heat exchanger model within a full system level model, computational time savings are critical.

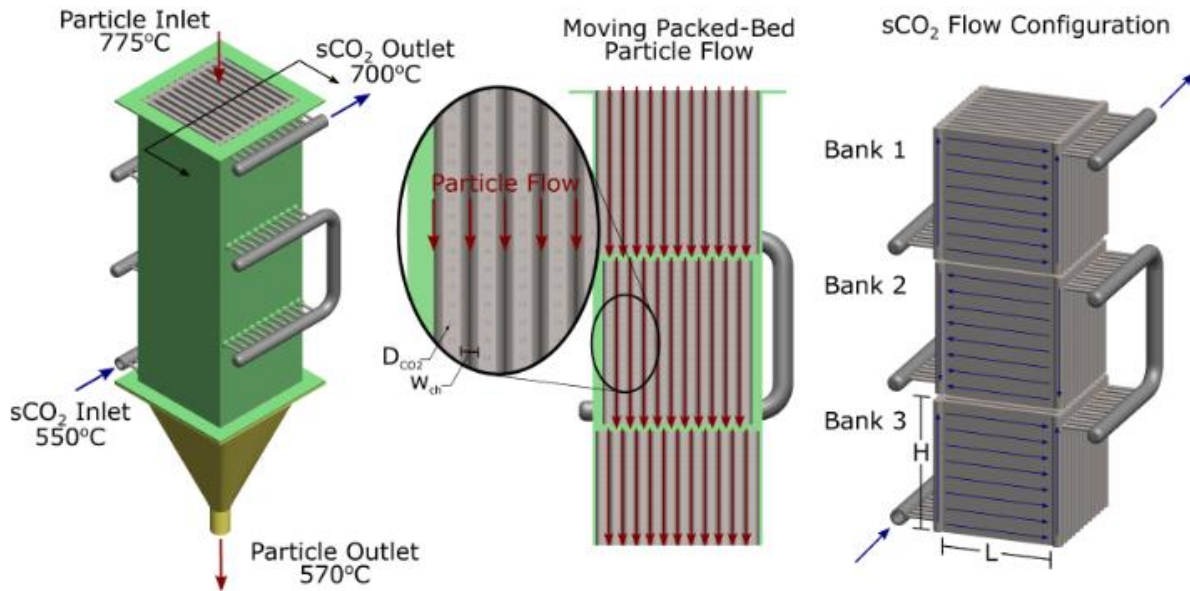


Figure 5: Diagram of a Particle-to-sCO₂ Moving Packed-Bed Heat Exchanger. sCO₂ in Blue and Particles in Red [9]

Table 1 lists the geometric and physical design properties of the heat exchanger. These values were taken from the work previously done by Fernández-Torrijos et al. In the moving shell and plate heat exchanger design used here, the particles flow vertically through a bank of channels around a series of horizontal pipes containing the sCO₂ stream. By placing multiple of these crossflow banks in series, the heat exchanger can be modeled as a counterflow heat exchanger. The flow characteristics and boundary conditions are detailed later as they change based on the experiment being run.

Table 1: Geometric and Physical Properties of Heat Exchanger

Parameter	Value
Heat Exchanger Height, H	1 [m]
Heat Exchanger Width, W	0.5 [m]
sCO ₂ Channel Width, w _{co2}	0.5 [mm]
Particle Channel Width, w _s	6 [mm]
Separation Plate Thickness, w _{HX}	1 [mm]
Plate Density, ρ _w	8238 [kg/m ³]
Plate Specific Heat, c _{pw}	468 [J/kgK]

The heat exchanger model is governed by a system of three partial differential equations [16]. These equations can be seen below where they solve for the temperature of the particles, T_s, supercritical carbon dioxide, T_{CO₂}, and wall, T_w. While there is air in the spaces between the particles, the stream was treated as being at thermal equilibrium instead of operating in a multiphase flow condition.

$$\rho_{s,b} C_{p,s,b} \frac{\partial T_s}{\partial t} = -\rho_{s,b} C_{p,s,b} \vec{u}_s \frac{\partial T_s}{\partial x} + \frac{2\bar{h}_{sw}}{w_s} (T_w - T_s) \quad (1)$$

$$\rho_{CO_2} C_{pCO_2} \frac{\partial T_{CO_2}}{\partial t} = -\rho_{CO_2} C_{pCO_2} \vec{u}_{CO_2} \frac{\partial T_{CO_2}}{\partial x} + \frac{2\bar{h}_{CO_2}}{w_{CO_2}} (T_w - T_{CO_2}) \quad (2)$$

$$\rho_w c_{pw} \frac{\partial T_w}{\partial t} = \frac{\bar{h}_{sw}}{w_{hx}} (T_s - T_w) + \frac{\bar{h}_{CO_2}}{w_{hx}} (T_{CO_2} - T_w) \quad (3)$$

The system of equations was discretized spatially using an upwind scheme and solved using a method of lines approach [25]. An important assumption about the heat exchanger model is the neglect of diffusion within the flow streams of the heat exchanger. To support this assumption, the Péclet number was calculated for the values shown in Table 2.

$$\begin{aligned} \text{Pe}_s &= \frac{L * \vec{u}}{\alpha} = 11263 \\ \text{Pe}_{\text{CO}_2} &= 2670000 \end{aligned} \quad (4)$$

A key component of these equations are the convection coefficients where the particles and gas interact with the heat exchanger walls. The particle to wall coefficient, \bar{h}_{sw} , was taken from Albrecht and Ho's 2D model [17]. This value is not temperature dependent and is approximated to be 150 W/(m²K). The sCO₂ to wall heat transfer coefficient is solved using the Gnielinski correlation based on the hydraulic diameter which is shown in equation 5.

$$\text{Nu}_{\text{Dh}} = \frac{\frac{f}{8} (\text{Re}_{\text{Dh}} - 1000) \text{Pr}}{1 + 12.7 \left(\frac{f}{8}\right)^{1/2} (\text{Pr}^{2/3} - 1)} \quad (5)$$

An initial test was run for 25 minutes of simulated time, and the boundary conditions and fluid properties can be seen in Table 2. After 2 minutes the inlet temperatures for the particles and sCO₂ were each lowered by 50 °C to check the model's ability to handle transient boundary conditions.

Table 2: Boundary Conditions and Flow Physical Properties for Initial Heat Exchanger Test

Parameter	Value
Particle Inlet Temperature Initial	775 [°C]
sCO ₂ Inlet Temperature Initial	550 [°C]
Particle Inlet Temperature After 2 Minutes	725 [°C]
sCO ₂ Inlet Temperature After 2 Minutes	500 [°C]
Heat Exchanger Wall Initial Temperature	650 [°C]
Particle Mass Flow Rate	0.02 [kg/s]
sCO ₂ Mass Flow Rate	0.0267 [kg/s]
Particle Bulk Heat Capacity	1200 [J/kg-K]
sCO ₂ Heat Capacity	1200 [J/kg-K]
Bulk Particle Density	2000 [kg/m ³]
sCO ₂ Density	200 [kg/m ³]

The results of this can be seen in Figures 5-7. These figures show the evolution of the temperatures for the particles, sCO₂ and wall over the 25-minute simulation run time. The particles enter the heat exchanger at x=0 and sCO₂ enters at x=1. After 10 minutes the temperatures start to approach a steady state and fully achieve steady state by the end of the test at 25 minutes.

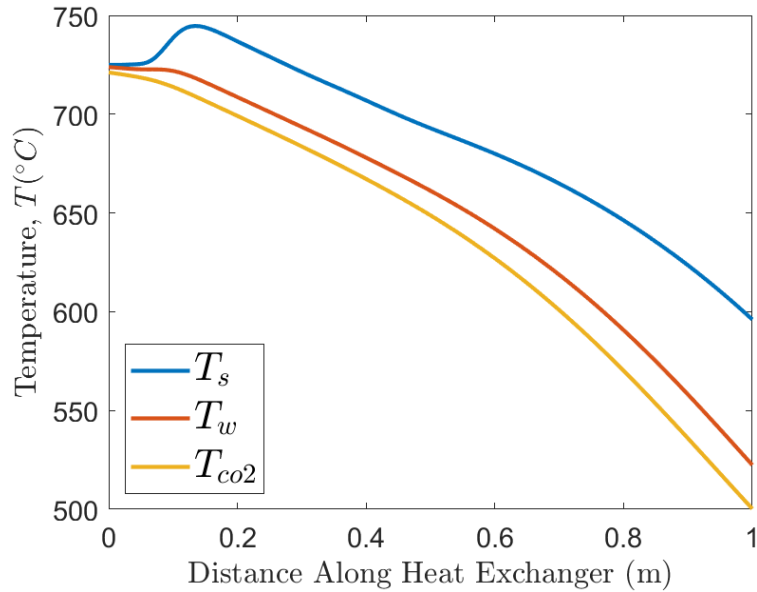


Figure 6: Particle, sCO₂ and Wall Temperatures 2.5 Minutes

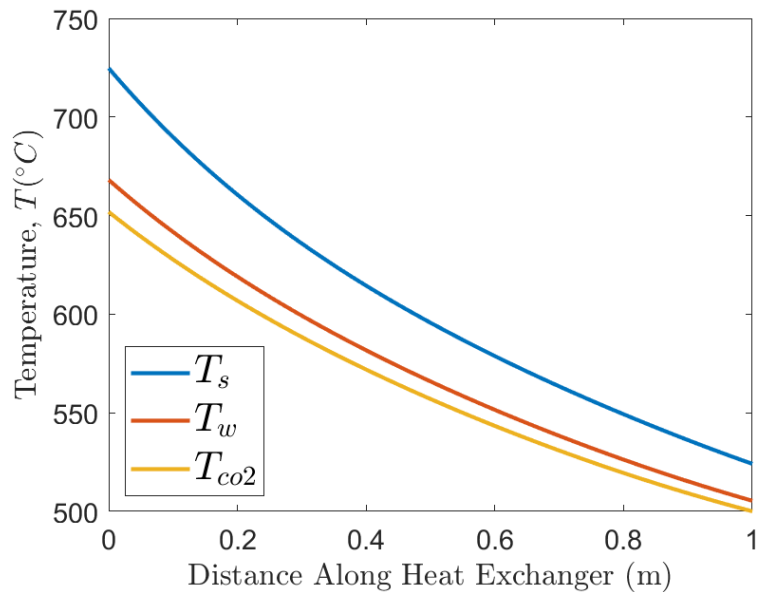


Figure 7: Particle, sCO₂ and Wall Temperatures 10 Minutes

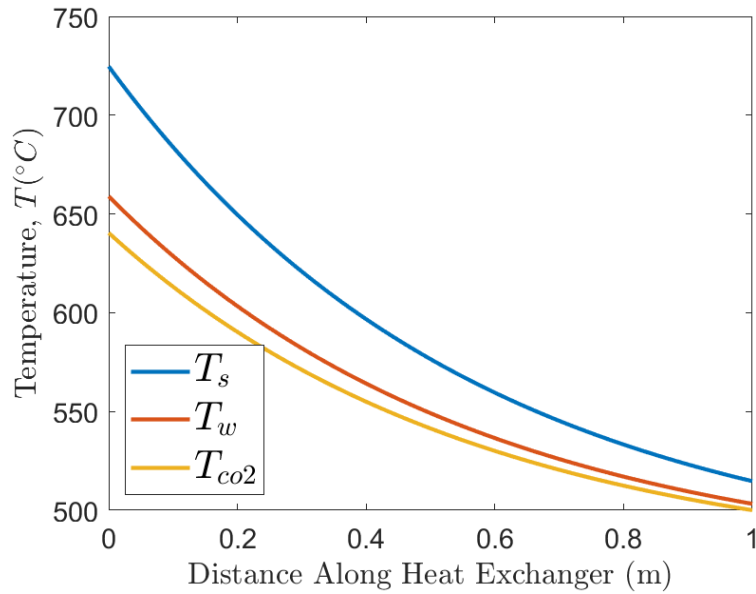


Figure 8: Particle, sCO₂ and Wall Temperatures 25 Minutes

Figure 6 captures the heat exchanger 30 seconds after the inlet temperatures of both the particle and sCO₂ streams are lowered by 50°C. The bump seen in the particle temperature profile before $x=0.2$ is the remaining higher temperature particles moving through the system. By figure 8 the, the temperature change has moved through the system and the temperatures along the heat exchanger have reached steady state. Lowering both temperature inlets by 50°C results in the gas outlet temperature at $x=0$ being approximately 75 degrees lower than the initial temperature seen in Figure 6. Another characteristic shown within this series of figures is the higher heat capacity rate of the sCO₂ stream. Over the length of the heat exchanger, the particles experience a 200°C drop versus a 150°C rise in the sCO₂ stream. This is an expected outcome where both streams have similar specific heats, but the sCO₂ stream has a higher mass flow rate. As an additional effect, the wall temperature profile is closer to that of the gas stream than the particle stream.

These results are in line with those presented by Fernández-Torrijos et al., as a part of their computational modeling work [16]. To further expand on the work completed by Fernández-

Torrijos et al., sensitivity analyses were completed to study the effects of various parameters on the outlet temperatures and wall temperature of the heat exchanger.

Table 3: Particle, sCO₂ and Wall Temperatures 25 Minutes

$T_{CO_2,In}$	$T_{p,In}$	\vec{U}_{CO_2}	\vec{U}_p	h_{sw}	$T_{CO_2,out}$	$T_{p,out}$	T_{wall}
550 °C	775 °C	0.54 m/s	0.0034 m/s	150 W/m ² K	703 °C	572 °C	614 °C

Table 4: Sensitivity Analysis Results of Heat Exchanger

Variable	Value	$T_{CO_2,out}$ (°C)	$T_{p,out}$ (°C)	T_{wall} (°C)
$T_{CO_2,In}$ (°C)	495 (-10%)	686 (-2.5%)	522 (-9.6%)	574 (-6.9%)
$T_{CO_2,In}$ (°C)	605 (+10%)	720 (+2.4%)	622 (+8.0%)	653 (+5.9%)
$T_{p,In}$ (°C)	698 (-10%)	650 (-8.1%)	565 (-1.2%)	592 (-3.7%)
$T_{p,In}$ (°C)	853 (+10%)	757 (+7.1%)	580 (+1.4%)	636 (+3.5%)
\vec{U}_{CO_2} (m/s)	0.432 (-20%)	727 (+3.3%)	587 (+2.6%)	645 (+4.8%)
\vec{U}_{CO_2} (m/s)	0.648 (+20%)	683 (-2.9%)	565 (-1.2%)	595 (-3.2%)
\vec{U}_p^* (m/s)	0.00272 (-20%)	683 (-2.9%)	560 (-2.1%)	590 (-4.1%)
\vec{U}_p^* (m/s)	0.00408 (+20%)	721 (+2.5%)	590 (+3.1%)	640 (+4.1%)
h_{sw} (W/m ² K)	135 (-10%)	701 (-0.3%)	575 (+0.5%)	614 (0%)
h_{sw} (W/m ² K)	165 (+10%)	705 (+0.5)	570 (-0.4%)	613 (-0.2%)

Table 3 displays the base case for the heat exchanger. The variables under study were the inlet temperatures, T_{CO_2} and T_p , the particle and gas velocity, \vec{U}_{CO_2} and \vec{U}_p , and the particle to wall heat transfer coefficient, h_{sw} . Change in the outlet temperatures and wall midpoint temperatures were used as the measurement of effect. The magnitude of change is the more important factor rather than the direction of change as either a positive or negative change might be desired depending on the operational condition. Modifying the inlet temperatures had the greatest average effect on the tracked temperatures. Each variable was changed in increments of 10% until the outlet temperatures demonstrated a change greater than one percent. This is the expected outcome for a

heat exchanger where the primary driver of heat exchange between the two sides is the total temperature difference between the two fluids. The velocity of the particles and the CO₂ streams are also measured as these would be important controls for the system during operation. The velocity of the particles is marked in Table 4 since the particle to wall heat transfer coefficient is a static value within the model that does not change with particle velocity. However, as discussed earlier, the CO₂ to wall heat transfer coefficient is determined within the model via the Gnielinski correlation. To achieve a noticeable effect on the final temperatures, the velocities needed to be varied by 20% compared to 10% for the inlet temperatures. This is consistent with the relatively narrow flow channels for the particles and CO₂. Increasing the velocity does not have a large impact on the total mass able to flow through the system; hence a large increase in velocity is required to see a change in temperatures. As mentioned previously, the particle to wall heat transfer coefficient is a static value that is not calculated within the model. This coefficient value was varied separately from the particle velocity to make attempt to capture this coefficients impact. While the other variables were modified until yielding output values greater than 1%, h_{sw} was only changed by 10% regardless of the output greater. This was because greater values would have been unrealistic to operation. However, modifying the coefficient without changing the velocity has even less of an impact. The velocity appears not only as a part of the coefficient calculation, but also within the advective portion of the heat transfer equation. This is consistent with the work done by Albrecht and Ho in calculating this coefficient value [17]. They determined that the major factor in changing the value was increasing or decreasing the effective particle size which modifies the overall mass flowrate through the system.

The sensitivity analysis provides good insights to the model and for later system level modeling attempts. Temperature changes to the inlet streams creates bigger impacts on the output

streams of the heat exchanger. This is intuitive to the operation of the heat exchanger, but provides knowledge for the operation of the heat exchanger. During operation this means that holding the particle inlet temperature steady is an important factor. There is also the opportunity to separate a portion of the CO₂ stream for mixing with the heated gas after the heat exchanger. A mass percentage of the CO₂ stream would flow through the heat exchanger to be reheated, but then would be mixed with the remaining mass stream. This technique can be used to have a finer control over the final temperature of the CO₂ stream heading back into the power block. While modifying the flow rate of the particles alone did not achieve a large change in outlet temperatures, changing the particle and gas flow rate at the same time could induce the desired outcome. This impacts the design of the storage silos and their operation as well.

2.2 Particle Storage Silo

In particle-based CSP systems, there are two particle storage silos. There is a silo for heated particles coming from the solar receiver and a silo for particles that have passed through the particle to sCO₂ heat exchanger. The model presented in this paper focuses primarily on the hot storage silo, but is applicable to particle storage silos broadly. Figure 10 details a diagram of the layers within the storage silo including the insulation and particles.

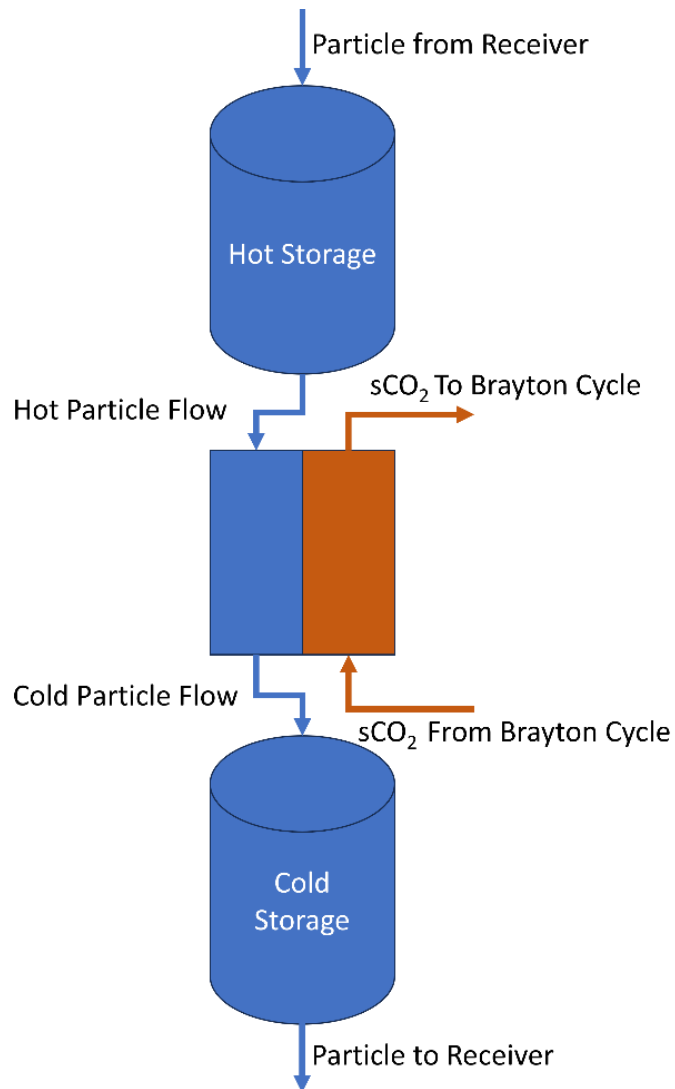


Figure 9: Diagram of Silo and Heat Exchanger Relative to CSP System

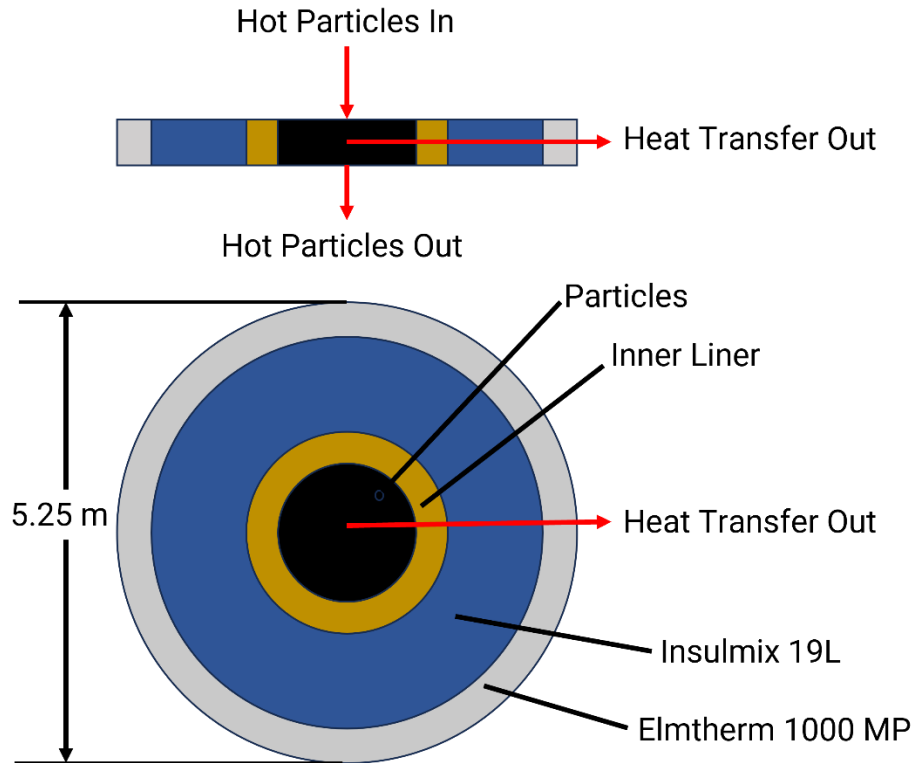


Figure 10: Top: Vertical Cross Section of Storage Silo. Bottom: Horizontal Cross Section of Storage Silo. Black: CARBO HSP 40/70, Yellow: Brick Inner Liner, Blue: Insulmix 19L, Gray: Elmtherm 1000 MP

The design of the silo itself closely follows the work presented by Sment et al. previously where the silo has a flat top, an angled bottom, and several layers of insulation [10,18]. This design presents several advantages. First, the flat top creates an insulating air pocket between the top of the particle stack and the inside of the silo roof. Second, the angled bottom reduces the overall weight of the silo because there are not stagnant particles within the silo. The weight of the silo could be of concern if the silos stay in line with the system to reduce the effort needed to transport hot particles. The critical dimensions of the stored particles are presented in Table 5 and the properties of the surrounding insulation are presented in Table 6.

Table 5: Geometric Dimensions of Stored Particles

Dimension	Value
Stored Particle Bed Diameter	4.3 [m]
Stored Particle Bed Height	5.5 [m]
Stored Particle Bed Mass	160000 [kg]

Table 6: Insulation Properties

Material	Conductivity [W/mK]	Thickness [m]
Brick Liner	1.53	0.0635
Insulmix 19L	0.15	0.381
Elmtherm 1000 MP	0.05	0.0254

The stored particle bed diameter is the diameter of the cylinder formed by the stored particles. Sment et al. propose a diameter of 4.3 m as the optimal diameter to minimize the surface area of the stored particles [18]. Stored particle height is found by calculating the height taken up by the total mass of stored particles with a cylinder and cone of a diameter of 4.3 m. Previous designs of storage silos had used a metal or concrete inner liner, but this was prone to damage due to the heat and abrasiveness of the particles. Current designs have switched to a brick layer on the inside to attempt to mitigate these problems [18]. A cross-sectional view of the storage silo can be seen in previously shown Figure 10.

In reality, the storage silo is split into two regions: a cylindrical portion and a conical shaped region. However, to simplify the model for use in later system level modeling, the silo is modeled as a straight cylinder. The silo is initially modeled in a steady state configuration where particles are not flowing in or out, but are only being held for 10 hours. Similarly to the heat exchanger, the particles and air in the void spaces are treated as a single-phase fluid.

$$\frac{\partial^2 T}{\partial x^2} - \frac{h_{\text{air}} P}{k_{s,\text{eff}} A_c} (T_s - T_\infty) = \frac{\rho_{s,b} C_{ps,b}}{k_{s,\text{eff}}} \frac{\partial T}{\partial t} \quad (6)$$

Equation 6 is the standard equation for capturing heat transfer through a constant cross-section fin. A_c is the conductive cross-sectional area [26]. For a typical fin, the convective heat transfer would be a function of the fin conductivity and fluid convection coefficient, but the layers of insulation complicate the model. In this model, the exterior air convection coefficient, h_{air} and the particle conductivity $k_{s,eff}$ are not the only relevant parameters present. The conductive resistances of the insulation layers are combined with these other terms from these parameters into an overall heat transfer coefficient, U . The solution for U can be seen in Equation 7.

$$U = 1 / \left[\frac{r_{particle}}{k_{brick}} \ln \left(\frac{r_{brick}}{r_{particle}} \right) + \frac{r_{particle}}{k_{Insulmix}} \ln \left(\frac{r_{Insulmix}}{r_{brick}} \right) + \frac{r_{particle}}{k_{Elmtherm}} \ln \left(\frac{r_{Elmtherm}}{r_{Insulmix}} \right) + \frac{r_{particle}}{r_{Elmtherm} h_{outer}} \right] \quad (7)$$

The radii referenced in the previous equation are additive starting from the center of the silo. Meaning that the radius of the brick layer is the brick layer thickness plus the radius of the stored particle cylinder and so forth for the next layers. The result of this can be seen in equation 8 where the overall heat transfer coefficient is multiplied by the perimeter of the heat transfer area, P . As previously stated, the conductivity in the bed, $k_{s,eff}$, is calculated using the ZBS model. Further explanation of the ZBS model can be found in the work of Chung et al [15].

$$\frac{\partial^2 T}{\partial x^2} - \frac{U * P}{k_{s,eff} * A_c} (T_s - T_{air}) = \frac{\rho_{s,b} C_{ps,b}}{k_{s,eff}} \frac{\partial T}{\partial t} \quad (8)$$

The solution approach for this model is similar to the one presented in the heat exchanger section. A method of lines is applied where the spatial derivatives are discretized using a second order central difference scheme, but the temporal derivative are maintained as a continuous derivative. Equation 8 captures the temperature change overtime for the stored particle bed, but to connect this temperature to the walls through a series of thermal conductivity equations as seen in equation 9.

$$q = \frac{T_1 - T_2}{R_{layer}} \quad (9)$$

In equation 9, the heat transfer, q , is the total heat transfer going from the particle bed to the outer wall, and R_{layer} is the resistance of the wall layer between two points where the temperature is measured. Figure 11 shows the results of tracking the temperature of the particles and insulation over a 10-hour holding period using the model outlined here.

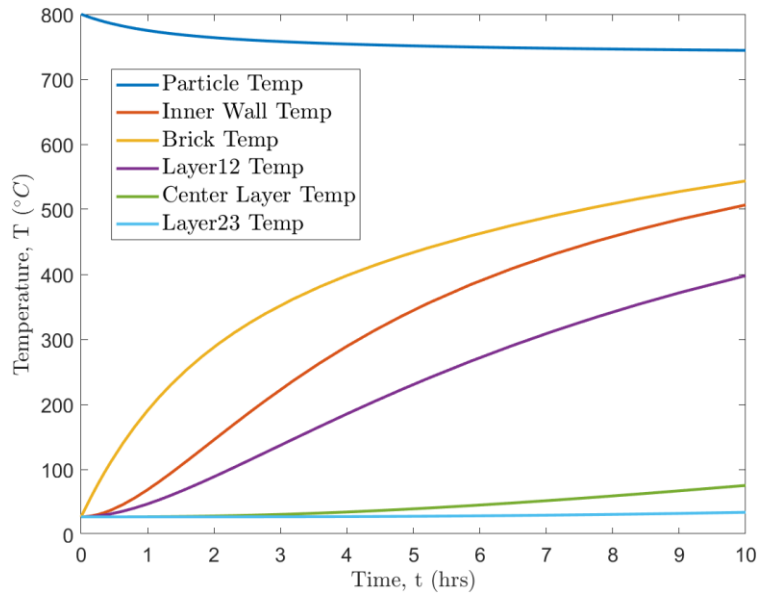


Figure 11: Temperature of Particles and Silo Insulation Over 10 Hours

For Figure 11, a particle bed was generated inside of the silo with a starting temperature of 800°C. The particles are then left to sit for 10 hours of simulated time to observe the heat transfer out to the silo walls. Temperatures on the inner layers rise rapidly because they are thin and highly conductive. The outer layers take much longer to warm up due to their thickness and low thermal conductivity, however, this behavior informs the design of the transient thermal model. Also in Figure 10, the boundaries between layers are called out as “Layer 12” and “Layer 23” to track the temperature of these boundaries even though contact resistance is not considered in the model.

To validate the use of the resistance network in creating a one-dimensional model, a Biot number was calculated. The Biot number calculated for the storage silo as shown in Equation 10 below.

$$\text{Bi} = \frac{\frac{L}{k_s A_c}}{\frac{1}{UA_s}} \quad (10)$$

The Biot number in equation 10 is a ratio of the conductive resistance vertically through the packed particle bed and the overall resistance through the silo walls. In this model the Biot number comes out as 0.0248 which is less than 1 supporting the use of the quasi-1D "fin" model.

An important consideration when developing the transient model of the storage silo is capturing the temperature of the insulation layers. At steady state these temperatures could be captured using a simple resistance network, however, the thermal mass of the insulation will have an effect on the temperature of the particles over time [19]. To accurately model this concept, but maintain the quasi 1D nature of the model, thermal capacitors are added to the model [20]. Equation 11 represents the generalized form of a thermal resistance-capacitance model where R and C are the resistance and capacitance respectively

$$\frac{dq}{dt} + \frac{1}{RC}q + \frac{Q}{RC} = 0 \quad (11)$$

Q represents the total heat flux moving through the wall, while q is the heat flux moving to through either the thermal resistor or capacitor. The RC network used to capture this heat transfer through the wall is a modified form of the one presented in Figure 12 that was developed by Silva for use in building insulation [20].

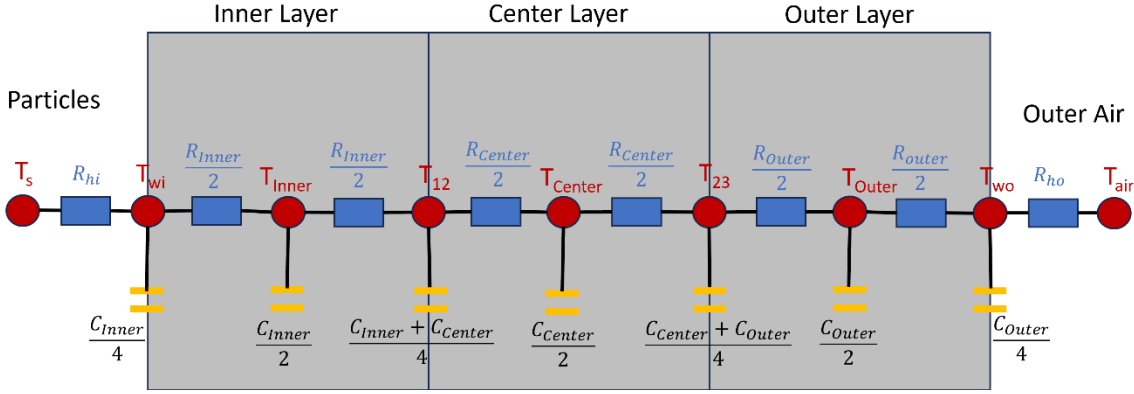


Figure 12: RC Network of a Silo Insulation Layers

In the case of the particle storage silo, T_s , being the temperature of the particles and T_{air} being the temperature of the outside air. The capacitances are sub divided to capture the different interactions between each layer of insulation where the capacitance of one layer will be shared with the surrounding layers. There are also intermediate nodes for where the layers meet each other and interact. Together this captures the capacitance effects of the insulation layers on both the particles and the silo wall itself. Equation 12 is a representative equation for the RC network in the wall. The capacitance, C , results from the layer thickness, material density, and material heat capacity. Also, the resistances between each temperature node are not perfectly divided in half since the layers are radial, but the value is close enough to half for this solution.

$$\frac{C_{Center}}{2} \frac{dT_{Center}}{dt} = \frac{T_{12} - T_{Center}}{R_{middle}/2} - \frac{T_{middle} - T_{23}}{R_{middle}/2} \quad (12)$$

Once the RC network is fully combined with the system modeled in Equation 8, the quasi-steady state model is formed which provides a picture of particles remaining in the silo for an extended duration, but periodically being replaced instantaneously.

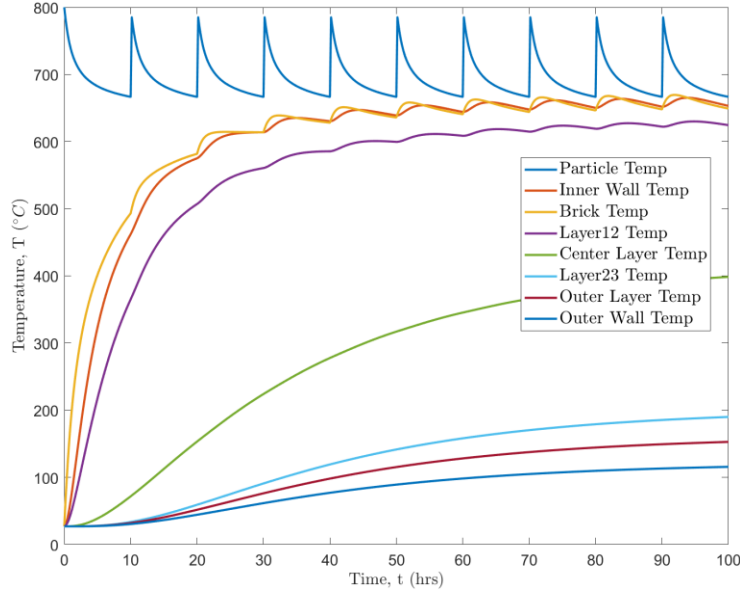


Figure 13: Temperatures of Stored Particles and Insulation Over 100 Hour in Quasi-Steady State

Figure 13 displays the temperature of the particles and insulation layers in the hot storage silo over 100 hours. Every 10 hours, the cooled particles are instantly removed and replaced with hot particles at the initial temperature of 800°C. The insulation layers experience spikes in temperatures at the same time as the particles are replaced due to this replacement with hot particles. This simulates a quasi-steady state situation and shows the thermal capacity effect of the insulation. This effect has been shown in previous work by Gifford et al [19].

The final steps in creating a fully transient model of the particle storage silo were the additions of advection to Equation 8 and solving continuity equations simultaneously. Equation 13 below shows the modification of the original heat transfer equation to include advection to the system.

$$k_{s,eff}A_c \frac{\partial^2 T_s}{\partial X^2} - \rho_{s,b} C_{ps,b} \bar{U}_s A_c \frac{\partial T_s}{\partial X} - PU(T_s - T_\infty) = \rho_{s,b} A_c C_{ps,b} \frac{\partial T_s}{\partial t} \quad (13)$$

Advection is added through the first order derivative term of particle temperature, multiplied by the density, heat capacity, and velocity of the particles. The velocity of the particles

is considered as the bulk vertical velocity of the particle bed to simplify the model creation process.

Results of these additions can be seen in Figures 14a and 14b.

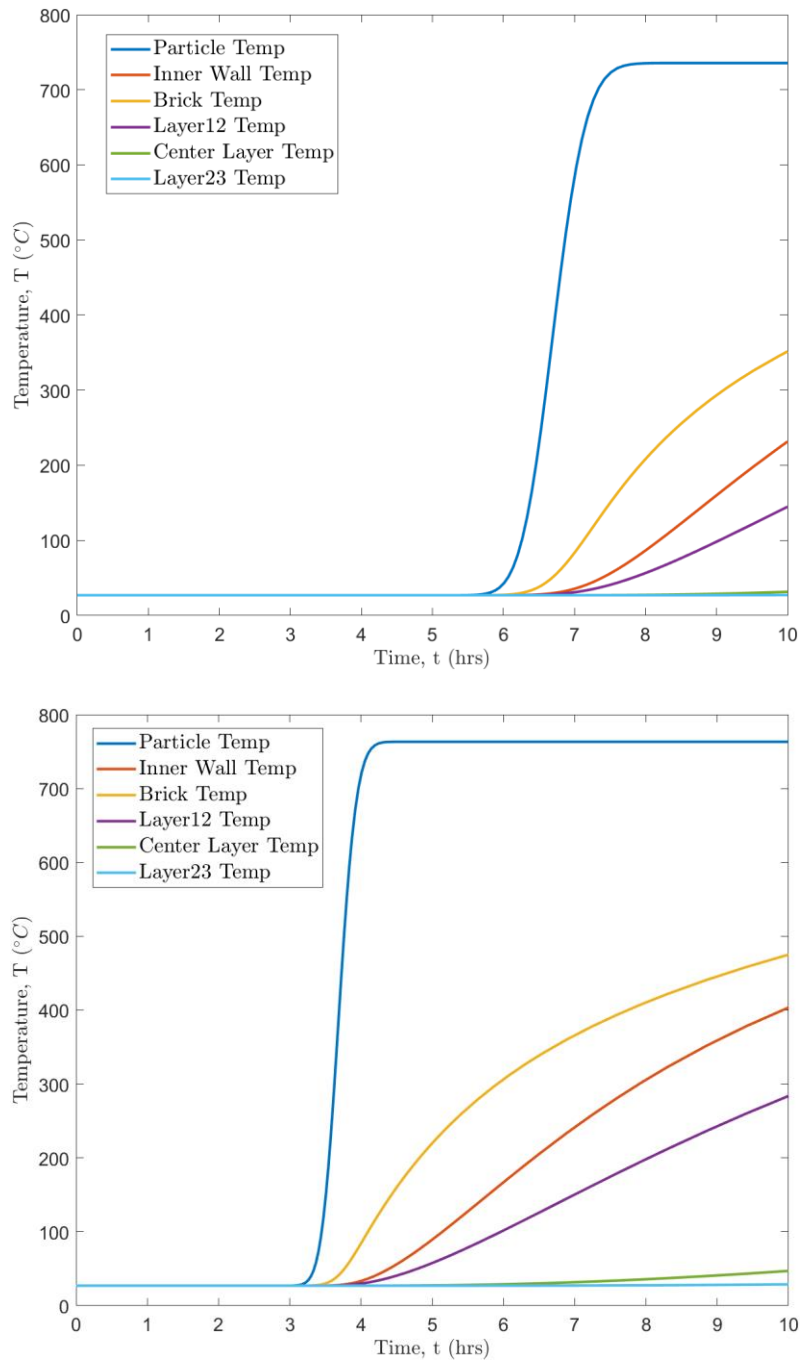


Figure 14: a) Top: Particle and Insulation Temperature after 10 Hours with Particle Velocity of 0.0033 m/s. b) Bottom: Velocity of 0.006 m/s

Figure 14 demonstrates the effects of modifying the speed at which the particles move through the storage silo. The system begins with everything starting at room temperature of 23 °C and then being replaced with particles leaving the solar receiver at 800 °C. As is expected the time it takes for the particle temperature to change decreases as the flow rate increases. The rate of change within the insulation layers is consistent with the results shown in the quasi-steady state analysis. This shows that the addition of advection does not significantly increase the rate of heat transfer from the particles to the surrounding insulation. This is in line with the work Albrecht and Ho completed for heat exchangers showing that modifying the particle size had a larger impact on the heat exchange than modifying the speed alone [17].

Similarly to the heat exchanger, sensitivity analysis work was performed for the storage model to determine what effects changing certain parameters would have on the temperatures in the storage silo.

Table 7 shows the base case for the storage silo. The considered parameters are analysis are the radius of the stored particle bed, as well as, the thickness of the insulation layers. These two variables were chosen since the advection results showed that factors like bulk particle bed velocity do not have a major impact on the heat transfer through the silo walls. To judge the effectiveness of changing the variables, the temperatures of the three insulation layers were used.

Table 7: Base Case for Storage Silo Sensitivity Analysis

r_p	th_{inner}	th_{middle}	th_{outer}	T_{inner}	T_{middle}	T_{outer}
2.15 m	0.0635 m	0.381 m	0.0254 m	761 °C	456 °C	172 °C

Table 8 displays the results of the sensitivity analysis. There are two important factors to consider about how the model is constructed when judging these results. First, in work by Sment et al, they demonstrated that maintaining the packed particle bed at a diameter to height ratio of

1:4 reduces the overall surface area exposed for heat transfer [18]. Within the model, this ratio is enforced meaning that as the diameter of the particle bed changes, so does the height of the storage silo. This results in fairly similar performance between tests even as the radius changes by half a meter in the positive and negative directions. The other factor to consider within the computational model is that the thickness of the insulation area all changes at the same rate. This was done to maintain consistency with the structural analysis work completed in previous works [10,18]. As is expected, increasing the thickness of the insulation layers decreases the overall temperature increases in the outer insulation layers. The temperature of the innermost insulation layer sees the least change overall compared to the starting temperature. This inner most layer is relatively thin and exists mostly to protect the middle insulation layer from coming into direct contact with hot ceramic particles which could damage the insulation material. From a design perspective this means there could still be opportunities to find a more insulative material for the inner layer that still provides protection from the abrasive particles. A similar effect occurs in the outer layer that shields the insulation from weather effects. The relatively thin layer of material reacts more drastically to changes in thickness than the thicker middle layer.

Table 8: Results of Storage Silo Sensitivity Analysis

Variable	Value	T _{inner} (°C)	T _{middle} (°C)	T _{outer} (°C)
r _p (m)	1.51 (-30%)	760 (-0.1%)	458 (+0.4%)	176 (+2.3%)
r _p (m)	2.79 (+30%)	762 (+0.1%)	455 (-0.2%)	170 (-1.2%)
Insulation (m)	0.423 (-10%)	764 (+0.4%)	472 (+3.4%)	186 (+7.5%)
Insulation (m)	0.517 (+10%)	758 (-0.4%)	436 (-4.6%)	158 (-8.9%)

There are fewer design insights gained from the particle storage sensitivity analysis than there were in the heat exchanger analysis. Comparatively, the storage silo is simpler than the heat exchanger with fewer variables to change. The demands on the particle storage silo are dictated primarily by other components within the CSP system. Inlet particle temperature and velocity are

determined at the receiver level. The particle velocity out of the silo is determined by the needs of the heat exchanger and power block. Work by other groups show that in the design stage there are more variables to consider, but once in operation the silo is a fairly stable system. The next step within this analysis is to look at the outcomes of combining the storage silo and heat exchanger sub components into one continuous subsystem.

CHAPTER 3: COMBINED SYSTEM MODEL AND EXERGY ANALYSIS

To progress toward the long-term goal of a full system level model, the next step in the project was the integration of the heat exchanger with the storage silo. The objective here was to flex the model further and see if any new behaviors appeared in either component or in the combined system. This combined model also generates insights for future developers when trying to create control schemes for the full CSP system. Along with the creation of this combined subsystem, exergy analysis was also performed on the subcomponents and the combined system. Exergy analysis can be used to determine the true efficiency of a specific system by comparing the effectiveness of the real system to the ideal system. First law efficiency compares the real system to the ideal version. A second law approach can give a more accurate picture as the second law efficiency compares the system at the current state to the maximum possible potential of the system. This is to say that whereas first law analysis assumes a system might be 100% efficient based upon full conversion of input energy, a second law analysis would evaluate a system based upon thermodynamic limitation of the quality of energy. Such energy quality is captured via exergy which associates the work potential of energy. This exergy analysis can give a clearer picture of some of the outcomes discussed in chapter 2 as a part of the sensitivity analysis. The exergy destruction over time can also be tracked using the transient models developed.

3.1 Combined Heat Exchanger and Storage Silo

From a modeling perspective, to combine the two models the inputs and outputs of each subcomponent needed to be connected. In this case, the temperature and mass flow rate exiting the storage silo became the inlet boundary conditions for the particle side of the heat exchanger. The storage inlet temperature would come from the receiver in the full system, but for this work

changes in the inlet temperature are simulated to model various effects on the receiver like sudden cloud cover. A similar effect occurs for the sCO₂ side of the heat exchanger. Without simulating a full sCO₂ Brayton cycle, the outlet temperature from the heat exchanger has no impact on the inlet temperature. Changes in the inlet temperature were simulated to reflect different power demands of the Brayton cycle where the turbomachinery might be operating at different levels. Figure 15 below displays a diagram of these connected variables.

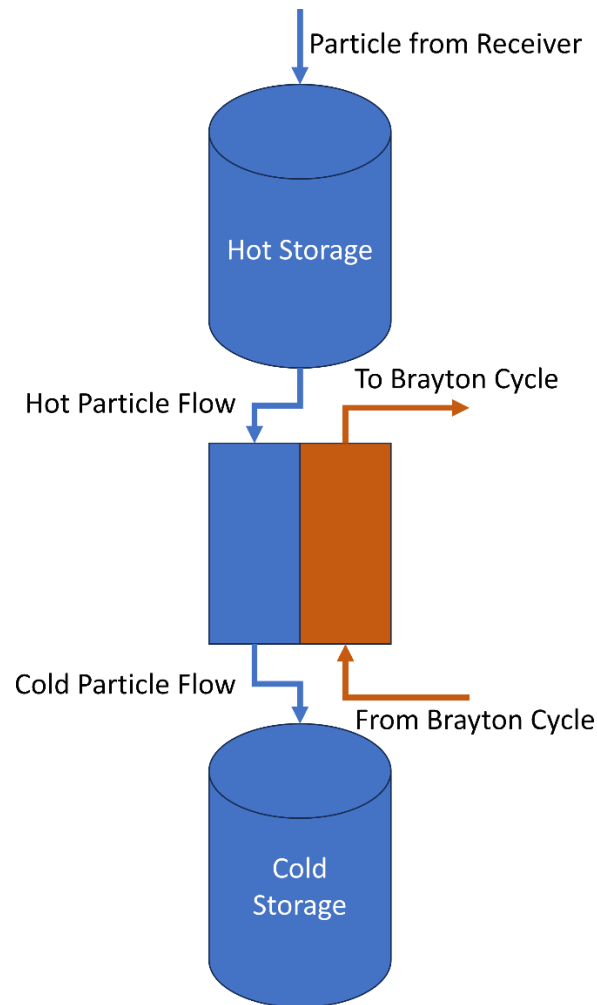


Figure 15: Diagram of Mass Flows in Combined Storage and Heat Exchanger System

In Figure 15, the particle mass flow follows the blue path from the solar receiver, into the hot storage silo modeled in section 2.2, through one side of the heat exchanger from section 2.1, and out into a cold storage silo. The sCO₂ follows the orange path from the Brayton cycle,

exchanges heat with the particles and then flows back to the Brayton cycle. In this configuration, there are no external controls imposed on the system compared to a fully realized system that might have dynamic controls on the flow rate of sCO₂ or particles into the heat exchanger. The results in this section will come from modifying the input conditions to the subsystem and letting the subsystem naturally respond

Table 9: Base Case for Combined System Modeling

Variable	Value
Particle Inlet Temperature	775 °C
sCO ₂ Inlet Temperature	550 °C
Particle Mass Flow Rate	0.02 kg/s
sCO ₂ Mass Flow Rate	0.0267 kg/s

Table 9 shows the boundary conditions for the heat exchanger and storage silo for a base case where the flow rates and temperatures are constant throughout the run time. The base case values are the same values used in the heat exchanger sensitivity analysis to establish a baseline there. All of the cases are run for 10 hours to capture the system running through peak daytime hours. Figures 16 and 17 show the temperatures in the storage silo and heat exchanger for this case.

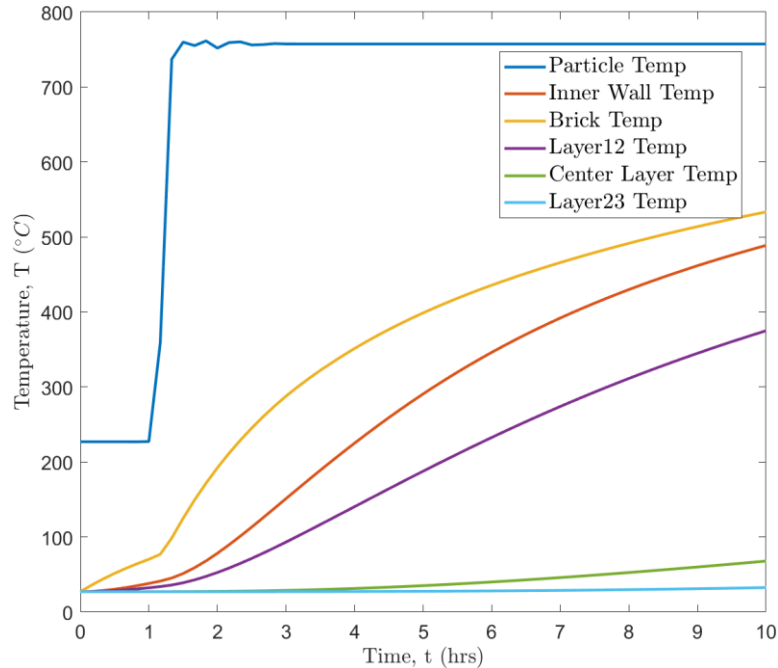


Figure 16: Particle and Insulation Temperatures for Storage Silo Over 10 Hours

Figure 16 demonstrates the temperature change over time for a hot storage silo where there are particles initially at 225°C already in the silo. The silo insulation material begins at 25°C before the hot particles are added. Temperatures for the particles and silo material are measured at the bottom of silo leading to the flat line present in the particle temperature at the start of the simulation. At a particle mass flow rate of 0.02 kg/s, the particles take approximately 1 hour to move from the top of the silo to the bottom of the silo creating the temperature spike seen in figure 16. While the inner most layers of insulation begin to heat quickly once the hot particles reach the silo, the center layer and beyond take significantly longer to show any change. The outer insulation layer and outer wall of the silo are not graphed in Figure 16 as they show no change over the 10-hour run time. This leads to the conclusion that during the initial start-up sequence for the CSP plant, hot particles will need to be run through the silo for several days to bring up the insulation material up to temperature in order to reduce heat loss from the particles.

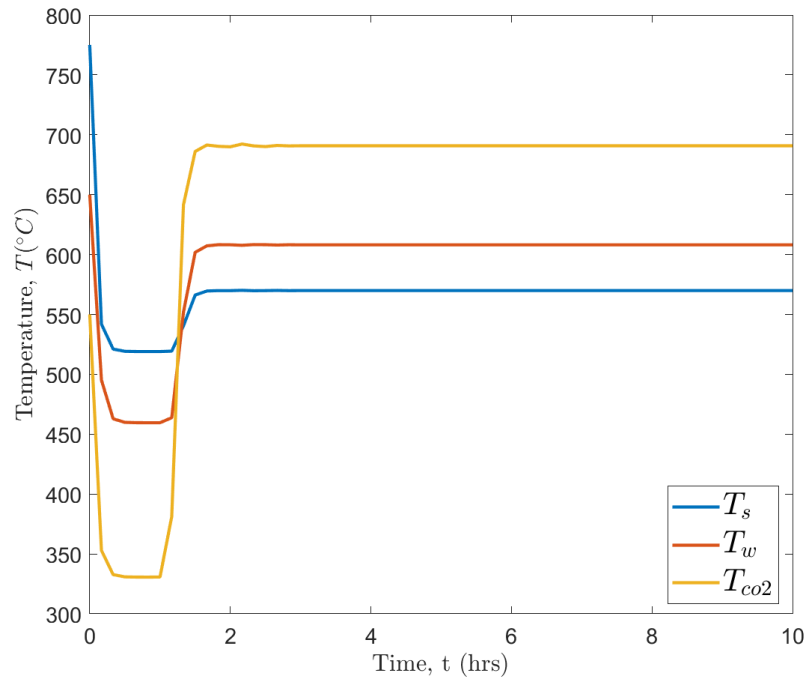


Figure 17: Heat Exchanger Outlet Temperatures for Combined System

Figure 17 shows the effects on the heat exchanger connected to the storage silo that was plotted in Figure 16. A similar drop can be seen in all three plotted values where the temperatures drop to the level of the particles that were in the storage silo at the start. After that initial one hour the heat exchanger rises to the steady state temperatures demonstrated within the original modeling of section 2.1. Again, the temperature diagrams shown in both figures are indicative of a startup process where the CSP system is filled initially with particles pre-heated by some other method before flowing through the receiver to reach standard operating temperatures.

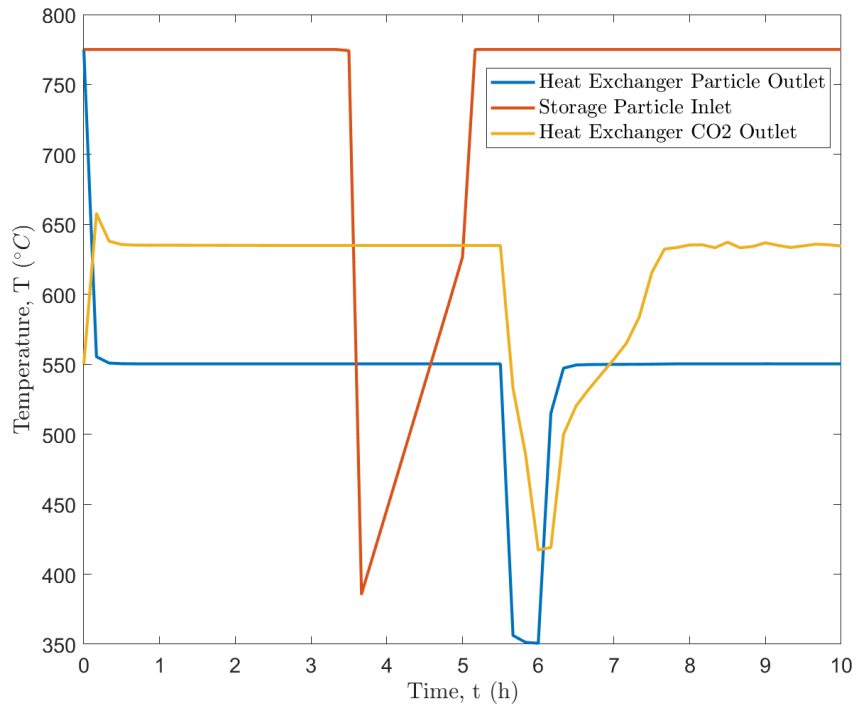


Figure 18: Particle Flow Decreased to 0.01 kg/s, Inlet Temperature Drop to 375°C and Then Rise over 1.5 Hours, sCO₂ Inlet Dropped by 200°C

Figure 18 models a system in which the particle flow has been reduced to 0.01 kg/s, the storage inlet temperature drops to 375°C and then steadily rises over the following 1.5 hours to 650°C before returning to the original inlet temperature, and the sCO₂ inlet temperature is artificially lowered by 200 °C to model the impact of a lower outlet temperature. A sudden drop in the inlet temperature to the storage silo could occur when clouds cover the heliostat field. This leads to a large and fast drop of the temperature of the particles exiting the receiver due to the reduced solar irradiation. Since the particle mass flow rate is half of the original base case, there is a much longer delay in the particles reaching the heat exchanger. A change in the particle mass flow rate could be driven by a reduced particle flow through the receiver segment of the full CSP system. For a scenario where the incoming solar irradiation for the receiver has dropped, a plant operator might want to reduce the particle flow rate to supply as much heat to the particles as possible. In the base case, the particles reach the heat exchanger inlet after an hour, but in this case

the particles take an hour longer. Artificially lowering the inlet temperature for the sCO₂ is required to simulate some effect of the fluid moving through the Brayton cycle that is not present in this model testing.

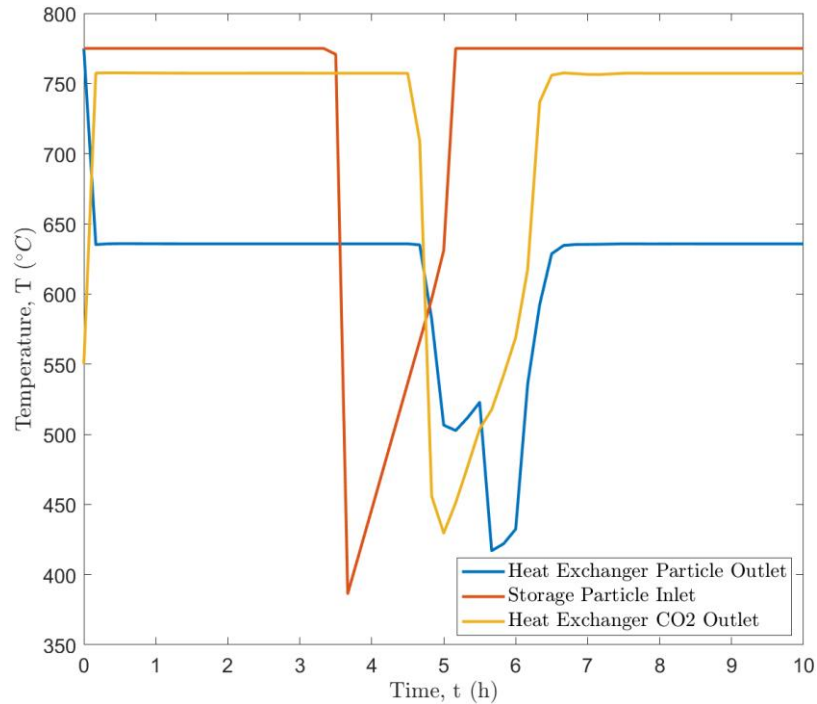


Figure 19: Particle Flow Back to 0.02 kg/s, sCO₂ Flow Decreased to 0.01335 kg/s, Same Temperature Change as Figure 18

Figure 19 models a similar system to the one demonstrated in Figure 18. The system operates under the same temperature transients presented in Figure 18, where the particle temperature drops to 375°C and the sCO₂ inlet temperature drops by 200°C in response. The particle flow rate has been changed back to the base rate of 0.02 kg/s. However, the flow rate of the sCO₂ was decreased by half to 0.01335 kg/s. In the sensitivity analysis portion of chapter 2.1, the flow rate of the sCO₂ was identified as a key way to control the temperature of the stream without any control over the inlet temperatures. By slowing the speed down, the sCO₂ spends more time in contact with the particles meaning that more heat is transferred. Even with the same drop in inlet temperatures, the sCO₂ reaches 100 degrees higher than the previous case. Another

important note is that temperature of the outlet particles is higher than in Figure 18. This would allow the particles to be reheated to working temperature with lower energy requirements.

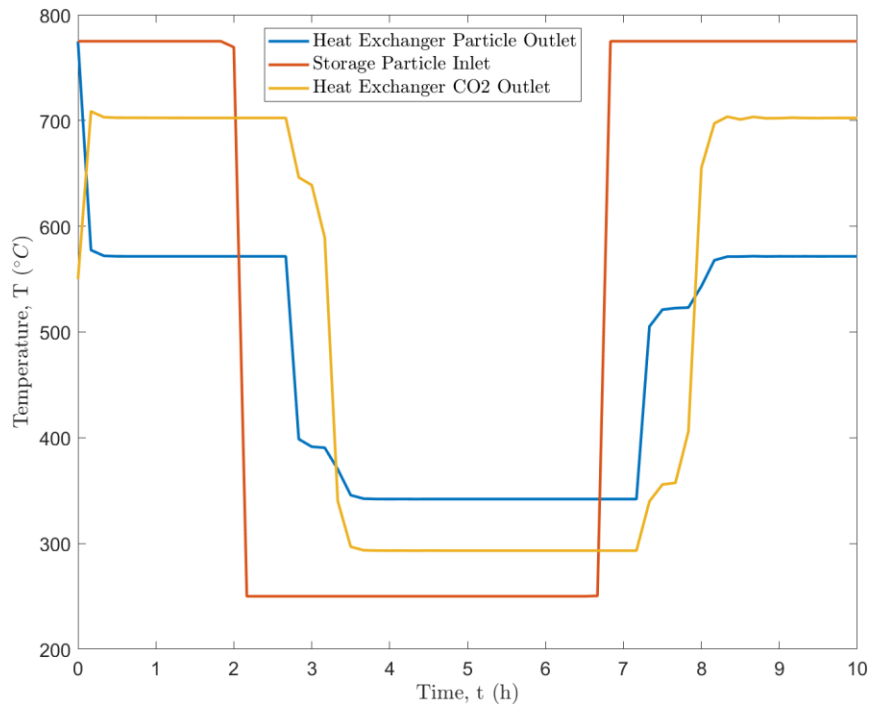


Figure 20: Particle and Gas Flow Return to Base Case, Inlet Temperature Dropped to 250°C for 4.5 Hours, sCO₂ Inlet Dropped by 200°C

Figure 20 captures the performance of a system similar to the base case where the only difference is a large temperature drop during the middle of the run as in the inlet particle temperature is decreased to 250°C. This case has phenomena present in both of the previous cases. The large drop in temperature is similar to the one shown in Figure 18, but without the gradual rise in temperature. In reality this happens when clouds rapidly cover the heliostat field and quickly uncover the field. Figure 19 also shows similar heat transfer performance to figure 19. However, due to the increased sCO₂ flow rate, the temperature does not reach as high of a point as the previous case.

For future control system designers, tracking the time delay between the particles entering the silo and then the heat exchanger is important feature. A plant operator could see the drop in

particle temperature coming and then either increase the particle flow rate or decrease the sCO₂ flow rate to maintain a constant power output from the Brayton cycle. These control designs can also be based around the known power demands downstream from the CSP plant. In the evenings where power demands increase, plant operators can plan to release particles ahead of time to generate more power. If there is control of the heliostat field, the inlet temperature to the particle storage can be controlled allowing for even earlier planning. The storage silo and the primary heat exchanger have been successfully coupled together. This is a major milestone in the process of creating a fully integrated CSP system. The final part of this work was to perform exergy analysis to determine the efficiency during steady state and under various load scenarios.

3.2 Exergy Analysis

According to Moran et al., exergy is the property that quantifies work potential within a system [21]. Unlike energy, exergy is not conserved and can be destroyed by the irreversibilities of a process. Exergy is useful in exploring the maximum work that can be extracted from a system when compared against the dead state of the environment. Equation 15 below is the general form of the exergy of a closed system at a specified state.

$$E = (U - U_0) + P_0 (V - V_0) - T_0 (S - S_0) + KE + PE \quad (15)$$

Exergy is comprised of the internal energy, volume, entropy, kinetic, and potential energy of the system. The 0 subscript denotes the values of the system at the dead state. A dead state system is defined at normal ambient conditions like 1 atm and 25°C. When the system is at rest at a reference point, the potential and kinetic energy terms are canceled. However, the systems being modeled in this work are open systems with mass crossing the boundary of the control volume. This requires the exergy equation to be modified to include the flow exergy which is the value of exergy carried by moving mass.

$$0 = \sum_j \left(1 - \frac{T_0}{T_j}\right) \dot{Q}_j - \dot{W}_{cv} + \dot{m}(e_{f1} - e_{f2}) - \dot{E}_d \quad (16)$$

Equation 16 is the exergy rate balance of an open system where \dot{E}_d is the exergy destruction and $\dot{m}(e_{f1} - e_{f2})$ is the flow exergy term. Flow exergy is further defined in equation 17 below.

$$e_f = h - h_0 - T_0(s - s_0) + \frac{V^2}{2} + gz \quad (17)$$

The flow exergy is the most important term for this work within exergy modeling. For the heat exchanger, the system is assumed to be adiabatic where heat transfer does not cross the control volume boundary. In the heat exchanger the work term is negated due to the lack of mechanical work and pressure change. The heat exchanger model simplifies to no pressure drop through the sCO₂ side of the heat exchanger and the particles have no change in pressure when moving through the system. The potential energy is orientation dependent for the heat exchanger. For the particles, there is a potential energy change since the particles need to fall through the heat exchanger. However, since the heat exchanger is designed for a crossflow configuration, the sCO₂ will not experience a change in potential energy. The control volume for defining exergy can be seen in Figure 21.

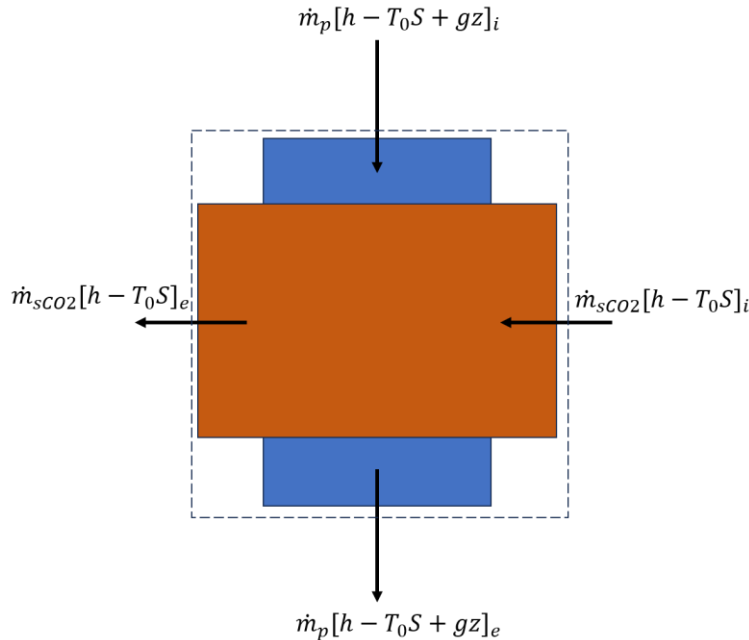


Figure 21: Control Volume Boundary of Heat Exchanger for Exergy Analysis

Using the inputs and outputs defined in the sensitivity analysis portion of chapter 2, the first step was performing exergy analysis on the individual components in a steady state configuration. The dead state for all tests was defined with T_0 at 25°C and P_0 at 1 atm. Table 10 defines the values for the exergy calculation for the heat exchanger.

Table 10: Exergetic Efficiency Analysis for Heat Exchanger Based on Lower Sensitivity Analysis from Table 4

Case #	$T_{CO_2,In}$ [C]	$T_{p,In}$ [C]	$T_{CO_2,out}$ [C]	$T_{p,out}$ [C]	\dot{m}_{CO_2} [kg/s]	\dot{m}_p [kg/s]	ϵ^* [%]
Case 1	550	775	703	572	0.0267	0.02	97.32
Case 2	495	775	686	522	0.0267	0.02	96.96
Case 3	550	698	650	565	0.0267	0.02	98.23
Case 4	550	775	727	587	0.0214	0.02	99.04
Case 5	550	775	683	560	0.0267	0.016	100

*Values at 100% caused by numerical rounding errors

Table 10 values are based on the lower percentile values developed in Table 4 of section 2.1. These values were chosen to expand upon the sensitivity analysis done there by comparing the effects of changing various input conditions on the steady state exergetic efficiency. Similar

trends that appeared in the original analysis appear here as well. Lowering the inlet temperature of the supercritical CO₂ decreases the efficiency of the system. A lower efficiency indicates a higher lost work potential within the heat exchanger. The closer the efficiency gets to 100 percent, more energy “quality” is also being transferred from the hot particle stream to the colder gas stream. Again, similar to previous results, slowing down the streams has the largest effect on the outcome. By keeping the same mass of a stream in the heat exchanger longer, more of the heat from the hot stream can be transferred into the colder stream.

Table 10 displays abnormally high efficiencies compared to what should be expected from conventional heat exchanger effectiveness. To verify the heat exchanger exergetic efficiency calculations within the model, the model was applied to the work of Fard et al., who were capturing the exergetic efficiencies of heat exchangers in a natural gas refinery [22-24]. The model used in this work was applied to several of the counterflow heat exchangers found with in Fard et al’s work. Table 11 shows the results of the of exergetic efficiency calculations from the model and from the cited work. Note that the majority of the heat exchanger within their work operate at temperatures below 600 K.

Table 11: Fard et al. Exergetic Efficiency vs Calculated Value [22-24]

Calculated Value	Value from Fard et al.	Heat Exchanger Tag No.
2.30%	0.87%	103-E-101 A/B
74.4%	75.7%	103-E-103
77.1%	77.3%	103-E-104
51.3%	50.3%	110-E-102
2.41%	1.44%	104-E-101
90.5%	88.5%	105-E-101A
26.4%	25.6%	114-E-108

The largest discrepancy between the model and cited values was a 1.5 (percentage point) difference between a calculated efficiency of 2.3% and an expected value of 0.87%. Note that Fard et al’s work also takes into account pressure drops within the fluids for their calculations of flow

exergy at the heat exchanger inlets and outlets, compared to this model where pressure drop is not considered. Another point of comparison is the exergetic efficiency for the heat exchanger configuration relative to their Log Mean Temperature Differences (LMTDs). The equation for LMTD used here can be seen in equation 18 below.

$$\text{LMTD} = \frac{\Delta T_A - \Delta T_B}{\ln(\Delta T_A) - \ln(\Delta T_B)} \text{ where } \begin{cases} \Delta T_A = T_{H,in} - T_{C,out} \\ \Delta T_B = T_{H,out} - T_{C,in} \end{cases} \quad (18)$$

The LMTDs for the cases shown in Table 10, as well as for the data taken from Fard et al.'s work can be seen in Table 12.

Table 12: LMTD for Cases Shown in Table 10 vs LMTD for Fard et al. Data

LMTD for Table 10 [C]	LMTD of Fard et al. [C]
42.1	32.3
51.9	60.5
28.3	41.9
42.2	56.0
36.9	15.5
No data	7.46
No data	31.0

As can be seen from Table 12, the particle to sCO₂ heat exchanger modeled for this work and the heat exchangers from Fard et al., operate at similar LMTDs. Given similar LMTDs, and the model agreement with exergetic efficiencies, it is possible to conclude that the presently given set of exergetic efficiencies are properly calculated. Results also seemed to indicate that the heat exchanger for this work exists with an asymptotically high region (i.e., with a ceiling of 100%). With the heat exchanger operating at high temperatures and with modest temperature differences across the streams, the efficiency extends into this region of greater than 95% efficiency. Part of this high efficiency could be explained by the model assuming near-perfect exergy transfer from the hot particle stream to the cold sCO₂ stream. In reality there would be significant contact resistance between the particle stream and the wall, increasing exergy losses during heat transfer.

However, the heat transfer model shown in chapter 2 does not consider this contact, but shows similar results to Albrecht and Ho's 2D modeling work [9]. Development of a more accurate exergy model for a particle heat exchanger is a topic for future work.

Another approach for validating the efficacy of the heat exchanger exergy model is to look at the entropy generation rate, S_{gen} , and the entropy generation number, N_s . Entropy generation number is a second law variant of the traditional NTU method for evaluating the performance of heat exchangers. Formulations for the entropy generation rate and the entropy generation number can be seen in equations 19 and 20 below for a system with no pressure drop.

$$\dot{S}_{gen} = \dot{m}_s c_{p,s,b} \ln \left(\frac{T_{s,o}}{T_{s,i}} \right) + \dot{m}_{co2} c_{p,co2} \ln \left(\frac{T_{co2,o}}{T_{co2,i}} \right) \quad (19)$$

$$N_s = \frac{\dot{S}_{gen}}{\dot{m}_s c_{p,s,b}} \quad (20)$$

Entropy generation rate can be used to describe the reversibility of a process where a number greater than 0 dictates an irreversible process. The entropy generation rate and number were calculated for the five heat exchanger cases used in the exergy analysis portion of this chapter. These results are displayed below in table 13.

Table 13: Entropy Generation Rate and Number for Modeled Heat Exchangers

Case Number	S_{gen} [kW/K]	N_s
1	0.3304	0.02
2	0.5241	0.02
3	0.1699	0.008
4	0.2535	0.01
5	0.3516	0.02

The results from table 13 line up with the exergetic efficiencies calculated for Table 10. Configurations that showed lower exergetic efficiencies had higher entropy generation rates, as

well as, higher entropy generation numbers. These results also give more supporting evidence for the accuracy of the exergetic efficiency model.

With exergy analysis performed on the heat exchanger individually, the final step was to perform a similar analysis on the combined system. Two separate exergy efficiencies were calculated for the combined sub-system. The definitions for these two efficiencies can be seen in the following equations.

$$\varepsilon_{wPO} = \frac{ef_{sCO2Outlet} + ef_{HxerParticleOutlet}}{ef_{sCO2Inlet} + ef_{StorageParticleInlet}} \quad (21)$$

$$\varepsilon_{woPO} = \frac{ef_{sCO2Outlet}}{ef_{sCO2Inlet} + ef_{StorageParticleInlet}} \quad (22)$$

Equation 21 defines the boundaries for the exergy calculation to include all of the inlets and outlets of the system. When the particles are flowing, they form a continuous system through the silo and out of the heat exchanger meaning there is not an exergy boundary between the outlet of the storage and in the inlet of the heat exchanger. This equation performs a full exergy accounting of the subsystem. Equation 22 drops the flow exergy term for the particle outlet in the heat exchanger. This gives a more direct portrait of the exergy that enters the system at the storage inlet and is transferred to the sCO₂ stream that feeds the power block. Both forms of efficiency are plotted below for multiple cases as a point of comparison.

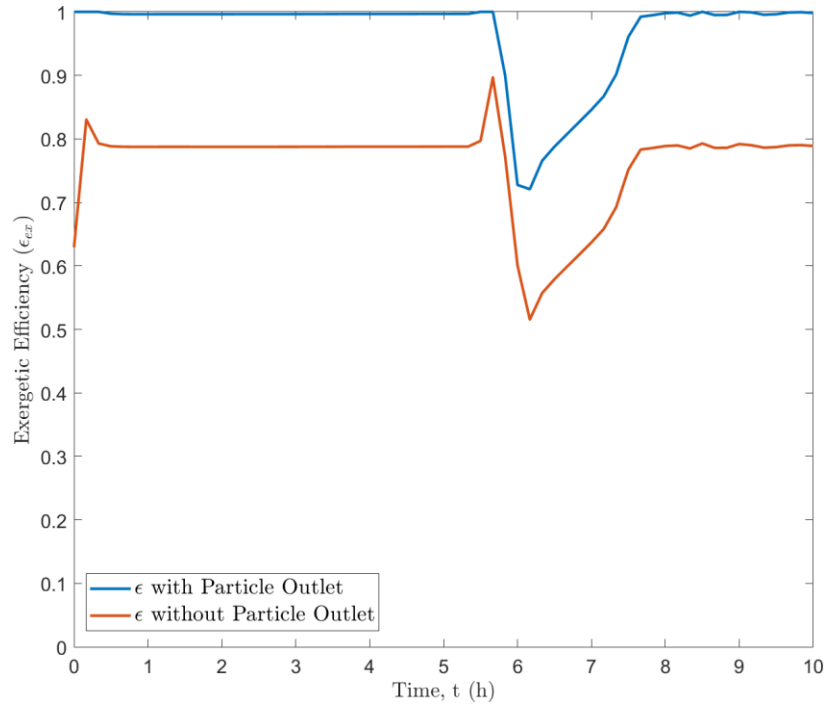


Figure 22: Exergy Efficiency for the Combined System Defined in Figure 18. Equation 21 in Blue. Equation 22 in Orange

Figure 22 plots both efficiencies defined in equations 21 and 22 for the configuration that was defined for Figure 18 previously. As a reminder in this configuration, the inlet temperature of the particles drops 350°C before rising slowly over 1.5 hours, the inlet temperature of the sCO₂ drops by 200°C, and the particle flow rate was reduced to 0.01 kg/s. Without accounting for the exergy at the particle exit of the heat exchanger, the efficiency of the system is around 80% until the change in inlet temperatures occurs, after which the efficiency drops briefly to 40%. This drop in efficiency occurs in the same period that the sCO₂ temperature change occurs meaning that the heat exchanger is the primary driver of exergetic efficiency changes in the system. This is further supported by the efficiency calculation that accounts for the particle exit maintaining near 100% efficiency except for during the temperature drops. An implication of this phenomenon is that exergy in the system is recycled heavily from the particle stream meaning that less energy will be required to reheat the particles on their next pass through the system.

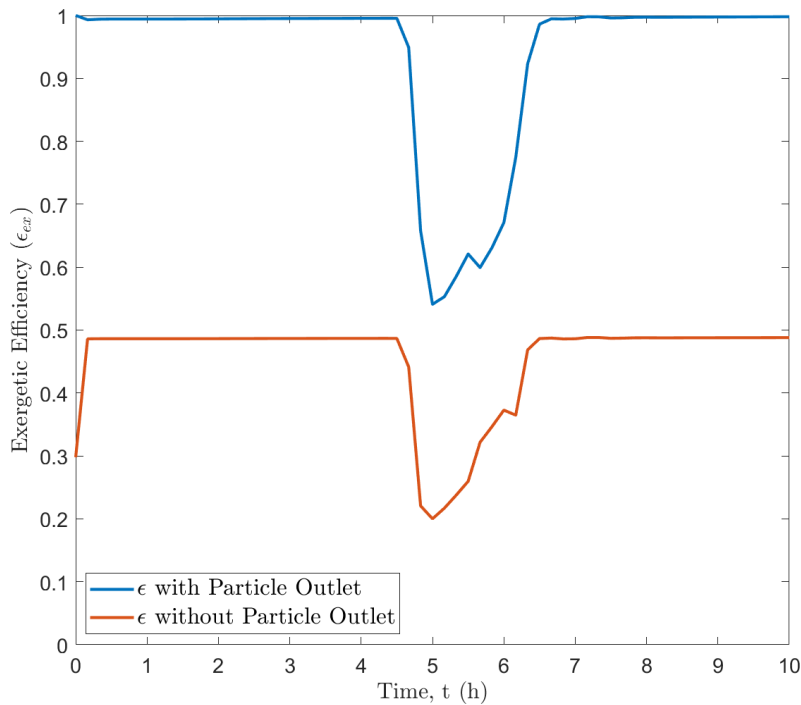


Figure 23: Exergy Efficiency for the Combined System Defined in Figure 19. Equation 21 in Blue. Equation 22 in Orange

For the configuration in Figure 19, the particles maintained the same 350°C temperature drop, along with the sCO₂ following the same 200°C drop from the previous case. However, the particle mass flow rate returned to 0.02kg/s and the sCO₂ rate dropped to 0.01335 kg/s. Once again, the flow efficiency calculation containing the particle outlet still rests near 100% outside of the temperature drop period. Without taking the particle outlet into consideration, the efficiency of the system is near 50% and decreases to 20% during the period of reduced temperatures. The flow rate of the sCO₂ has a much larger relative on the exergy transfer between the two streams, in the given case, than the particle flow rate did.

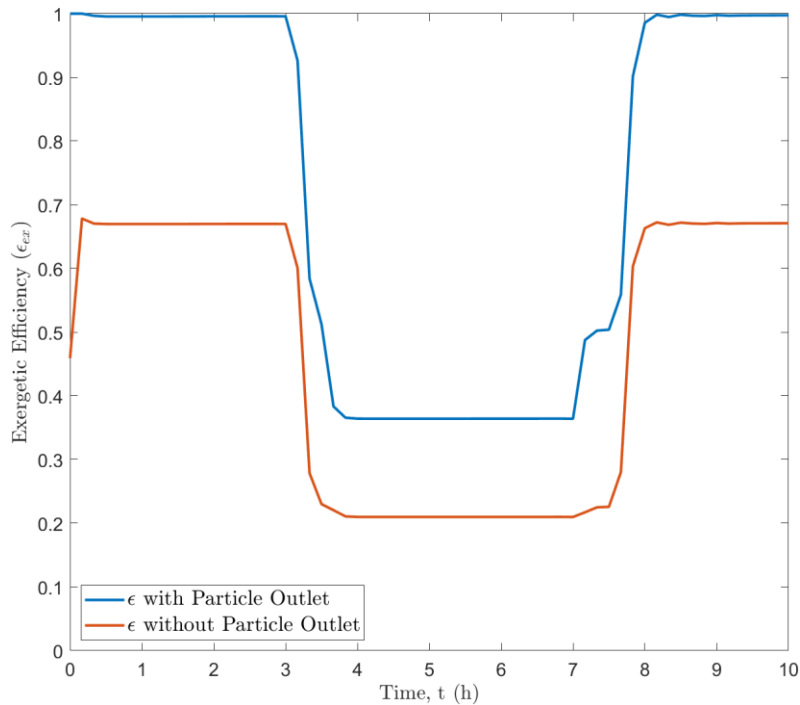


Figure 24: Exergy Efficiency for the Combined System Defined in Figure 20. Equation 21 in Blue. Equation 22 in Orange

Figure 24 follows the same configuration that was defined for Figure 20 where the particle mass flow rate is returned to 0.02 kg/s and the sCO₂ mass flow rate is returned to 0.0267 kg/s. However, the particle inlet temperature is lowered to 250°C during the middle part of the run time. The most interesting part of this case is that while the efficiency decreases to 20% like the example shown in Figure 23, the efficiency during the rest of the run rests in between the two values for Figures 22 and 23. For the operation of the combined system, the mass flow rates of the particles have a more dominant effect on the efficiencies of the system. This lines up with the formulation for exergetic efficiency which is highly dependent on mass flow rate.

These combined exergetic efficiency calculations have reinforced some of the previous conclusions regarding the operation of the combined sub system. Namely that the mass flowrates will be the primary means of controlling the response of the system. Large temperature swings generated the highest changes in exergetic efficiency, but these are not well controlled by the

system. The swings can be tempered on the sCO₂ side by mixing fluid passed through the heat exchanger with fluid separated from the main stream. On the particle side, controlling the mass flow rates is the only method for controlling the system and leveling out the impacts of large temperature swings in the particle stream.

CHAPTER 4: CONCLUSION

Previous work in this space has focused on the development of complex multi-dimensional models; however, there is a need for simpler component models. Simpler component models can then be combined into a full system level model that can run in real time for both the operation and development of CSP plants. The components developed here serve as the building blocks for future work on system level modeling and control. These models needed to be computationally simple, but still provide accurate results. To achieve this goal, a one-dimensional model of the particle storage silo was developed that could be coupled with a modified version of Albrecht and Ho's moving packed bed shell and plate heat exchanger model. Both of these components were investigated independently of each other and when coupled together in a continuous system. Sensitivity studies were performed on both components to determine which variables had the greatest impact on component performance. For the combined subsystem, various loads were applied to simulate the impacts of weather events on the CSP system. Finally, exergy analysis was performed to determine the efficiency of the subcomponents and combined system during operation. Overall, it was found that the inlet temperature of the particles had the biggest individual impact on the performance of combined storage-heat exchanger system.

Modeling of the heat exchanger was performed by modifying the model originally created by Albrecht and Ho. This model utilizes a one-dimensional method of lines approach where spatially the heat exchanger is discretized along the flow paths using an upwind scheme. In a method of lines approach, the time dimension is left as a continuous variable and the equations are solved within the MATLAB ODE solver. The inlet temperatures of the particles, as well as the mass flow rates, are used as the inputs for the system. Sensitivity analysis showed that within the heat exchanger, particle inlet temperature had the largest impact on the outlet temperature of the

sCO₂ stream. For a 10% change in inlet temperature, the sCO₂ stream demonstrated almost a 9% change in outlet temperature. The sCO₂ outlet stream was selected as the primary metric for judging performance in the sensitivity analysis as this value has a direct impact on the future power generation in a full scale CSP system.

The particle storage silo is computationally modeled in the same way as the heat exchanger with a one-dimensional method of lines. However, the silo model is quasi-one dimensional similar to finlike structures. To capture the heat transfer through the insulation layers of the silo wall, an RC network is coupled between the one-dimensional model of the packed particle bed and the outside air. This RC network also allows the transient effects of the insulation heat capacitance to be captured within the model. As the silo structure heats up overtime, the particles lose less heat to the structure material meaning that the outlet particles are closer in temperature to the inlet particles. Sensitivity analysis for the storage silo revealed that the insulation thickness had the largest impact on silo temperatures. This is an expected outcome where increasing the thickness lowers the final temperatures of the insulation layers. Changing the radius of the packed particle bed showed little impact (<2%) on the final temperatures. The primary reason for this is due to a condition within the model that forces a ratio between the diameter and height of the packed particle bed to reduce the exposed surface area. With this sensitivity analysis, a fully transient model of the particle storage silo was completed and could then be coupled to the heat exchanger.

Coupling the heat exchanger to the storage silo was a necessary step in the long-term goal of creating a full CSP system model. The heat exchanger receives particles at a temperature and mass flow rate equal to the outlet conditions of the storage silo. Particles enter the storage silo at a specified temperature from the solar receiver. Particles in the heat exchanger transfer heat to a sCO₂ stream before exiting to a second storage silo. Variable temperature profiles are applied to

the particles entering the storage silo to simulate the impacts of weather conditions on system performance. Again, using the outlet temperature of the sCO₂ as the primary indicator of system performance, the mass flow rate of the of the sCO₂ stream demonstrated the greatest impact on temperatures. While changes in the particle inlet had the greatest temporary effects, the sCO₂ mass flow rate had a greater impact over the 10-hour test. Slowing down the mass flowrate allowed the gas to stay in contact with the heated particles longer allowing for a greater amount of heat transfer. Changes to the particle mass flow rate had similar effects, but not to the same magnitude. Particle temperature is a hard variable to control, but the flow rates of both streams have options for active control. The sCO₂ side of the heat exchanger again shows more promise here since the stream could be split with only a portion of the total mass flowing through the heat exchanger. This heated portion could then be recombined with the rest of the mass stream to have a finer control on the final stream entering into the power block. These insights will help future designers of CSP plant controls in creating the control schemes for plants. These control schemes can be developed with the understanding that certain parameters, like the particle temperature or DNI, have a major impact on system temperatures, but are unable to be directly controlled. This leads to the plant designers looking for ways to indirectly control these areas. For example, the particle temperatures are not easily controlled, but the particle mass flow rates can be controlled at several points such as the outlet of the hot storage or the inlet into the receiver.

Exergy analysis was the final part of the work in this thesis. Exergy provides insights into the efficiency of the two components and the combined system. For the heat exchanger, exergetic efficiency was studied as this captures the work potential of the system. Overall, the heat exchanger had greater than 90% efficiency, but the model of the heat exchanger is not fully accurate. Pressure drop through the gas side is not captured, artificially increasing the efficiency of the system. For

the combined system, there were two separate exergetic efficiencies calculated. One calculation included the impacts of the particles exiting the heat exchanger and the other neglected this contribution. This was done to track the impact of the heat exchanger on the overall subsystem efficiency. It was found that the particle side of the heat exchanger has a major impact on the overall efficiency and recycles extensive exergy back into the overall system. A future area of study here would be the development of an exergy analysis that fully describes the system. This would need to include an exergy storage term for the silo, as well as, a more accurate method for describe exergetic efficiency within high temperature systems.

The final result of this work was the creation of heat exchanger and particle storage silo models that yield results similar to more complex works, but in a computationally less extensive method. While these models are not more accurate than previous models, they provide comparable results. There was no quantification of solution time of the 1D models compared to higher dimensional models, but intuitively the 1D model should solve faster due to the reduced dimension count. These models were shown to work well individually and when coupled together in one continuous subsystem. These models can then be taken and used inside of future system level CSP models to perform similar analyses at the system level. Future work should focus on the development of active control devices and schemes for managing the temperatures within the system. The work here focused on applying various stimuli to the components and letting them naturally respond. Once these component models are combined with models for the heliostat field, solar receiver, and power block, a full system level model can be created for plant designers and operators. CSP is an exciting avenue for renewable energy conversion, and chemical production and models like these will be critical in the further development of the field.

REFERENCES

- [1] A. H. Alami *et al.*, “Concentrating solar power (CSP) technologies: Status and analysis,” *International Journal of Thermofluids*, vol. 18, p. 100340, May 2023, doi: [10.1016/j.ijft.2023.100340](https://doi.org/10.1016/j.ijft.2023.100340).
- [2] M. T. Islam, N. Huda, A. B. Abdullah, and R. Saidur, “A comprehensive review of state-of-the-art concentrating solar power (CSP) technologies: Current status and research trends,” *Renewable and Sustainable Energy Reviews*, vol. 91, pp. 987–1018, Aug. 2018, doi: [10.1016/j.rser.2018.04.097](https://doi.org/10.1016/j.rser.2018.04.097).
- [3] M. Mehos *et al.*, “Concentrating Solar Power Gen3 Demonstration Roadmap,” National Renewable Energy Lab. (NREL), Golden, CO (United States), NREL/TP-5500-67464, Jan. 2017. doi: [10.2172/1338899](https://doi.org/10.2172/1338899).
- [4] M. V. Bagepalli, J. D. Yarrington, A. J. Schrader, Z. M. Zhang, D. Ranjan, and P. G. Loutzenhiser, “Measurement of flow properties coupled to experimental and numerical analyses of dense, granular flows for solar thermal energy storage,” *Solar Energy*, vol. 207, pp. 77–90, Sep. 2020, doi: [10.1016/j.solener.2020.06.062](https://doi.org/10.1016/j.solener.2020.06.062).
- [5] J.-M. Yin, Q.-Y. Zheng, Z.-R. Peng, and X.-R. Zhang, “Review of supercritical CO₂ power cycles integrated with CSP,” *International Journal of Energy Research*, vol. 44, no. 3, pp. 1337–1369, 2020, doi: [10.1002/er.4909](https://doi.org/10.1002/er.4909).
- [6] C. Turchi, “10 MW Supercritical CO₂ Turbine Test,” UNT Digital Library. Accessed: Jun. 07, 2024. [Online]. Available: <https://digital.library.unt.edu/ark:/67531/metadc866797/>
- [7] “Global energy transformation: A roadmap to 2050 (2019 edition).” Accessed: Jun. 07, 2024. [Online]. Available: <https://www.irena.org/publications/2019/Apr/Global-energy-transformation-A-roadmap-to-2050-2019Edition>
- [8] N. Blair *et al.*, “System Advisor Model (SAM) General Description (Version 2017.9.5),” NREL/TP-6A20-70414, 1440404, MainId:13734, May 2018. doi: [10.2172/1440404](https://doi.org/10.2172/1440404).
- [9] K. J. Albrecht and C. K. Ho, “Design and operating considerations for a shell-and-plate, moving packed-bed, particle-to-sCO₂ heat exchanger,” *Solar Energy*, vol. 178, pp. 331–340, Jan. 2019, doi: [10.1016/j.solener.2018.11.065](https://doi.org/10.1016/j.solener.2018.11.065).
- [10] J. Sment, K. Albrecht, M. J. Martinez, and C. K. Ho, “Design considerations for a high-temperature particle storage bin,” presented at the SOLARPACES 2019: International Conference on Concentrating Solar Power and Chemical Energy Systems, Daegu, South Korea, 2020, p. 190029. doi: [10.1063/5.0030505](https://doi.org/10.1063/5.0030505).

- [11] K. Plewe, J. N. Sment, M. J. Martinez, C. K. Ho, and D. Chen, “Transient thermal performance of high-temperature particle storage bins,” *AIP Conference Proceedings*, vol. 2445, no. 1, p. 160013, May 2022, doi: [10.1063/5.0085649](https://doi.org/10.1063/5.0085649).
- [12] Mathworks, “MATLAB.” The Mathworks Inc, Natick, Massachusetts, United States, 2023. [Windows 11]. Available: [mathworks.com](https://www.mathworks.com)
- [13] M. Inc, “Modelon Impact.” Modelon Inc, Lund, Sweden, 2024.
- [14] W. van Antwerpen, C. G. du Toit, and P. G. Rousseau, “A review of correlations to model the packing structure and effective thermal conductivity in packed beds of mono-sized spherical particles,” *Nuclear Engineering and Design*, vol. 240, no. 7, pp. 1803–1818, Jul. 2010, doi: [10.1016/j.nucengdes.2010.03.009](https://doi.org/10.1016/j.nucengdes.2010.03.009).
- [15] K. M. Chung *et al.*, “Measurement and analysis of thermal conductivity of ceramic particle beds for solar thermal energy storage,” *Solar Energy Materials and Solar Cells*, vol. 230, p. 111271, Sep. 2021, doi: [10.1016/j.solmat.2021.111271](https://doi.org/10.1016/j.solmat.2021.111271).
- [16] M. Fernández-Torrijos, K. J. Albrecht, and C. K. Ho, “Dynamic modeling of a particle/supercritical CO₂ heat exchanger for transient analysis and control,” *Applied Energy*, vol. 226, pp. 595–606, Sep. 2018, doi: [10.1016/j.apenergy.2018.06.016](https://doi.org/10.1016/j.apenergy.2018.06.016).
- [17] K. J. Albrecht and C. K. Ho, “Heat Transfer Models Of Moving Packed-Bed Particle-To-sCO₂ Heat Exchangers,” 2017.
- [18] J. Sment, K. Albrecht, J. Christian, and C. K. Ho, “Optimization of Storage Bin Geometry for High Temperature Particle-Based CSP Systems,” in *ASME 2019 13th International Conference on Energy Sustainability*, Bellevue, Washington, USA: American Society of Mechanical Engineers, Jul. 2019, p. V001T03A008. doi: [10.1115/ES2019-3903](https://doi.org/10.1115/ES2019-3903).
- [19] J. Gifford, Z. Ma, and P. Davenport, “Thermal Analysis of Insulation Design for a Thermal Energy Storage Silo Containment for Long-Duration Electricity Storage,” *Front. Energy Res.*, vol. 8, Jun. 2020, doi: [10.3389/fenrg.2020.00099](https://doi.org/10.3389/fenrg.2020.00099).
- [20] D. Silva, “Modeling the Transient Response of Thermal Circuits,” *Applied Sciences*, vol. 12, no. 24, Art. no. 24, Jan. 2022, doi: [10.3390/app122412555](https://doi.org/10.3390/app122412555).
- [21] M. J. Moran, H. N. Shapiro, D. D. Boettner, and M. B. Bailey, Eds., *Fundamentals of engineering thermodynamics*, 9th edition. Hoboken, NJ: Wiley, 2018.
- [22] M. Mehdizadeh-Fard, F. Pourfayaz, and A. Maleki, “Exergy analysis of multiple heat exchanger networks: An approach based on the irreversibility distribution ratio,” *Energy Reports*, vol. 7, pp. 174–193, Nov. 2021, doi: [10.1016/j.egyr.2020.11.166](https://doi.org/10.1016/j.egyr.2020.11.166).
- [23] M. Mehdizadeh Fard, F. Pourfayaz, A. B. Kasaeian, and M. Mehrpooya, “A practical approach to heat exchanger network design in a complex natural gas refinery,” *Journal of*

Natural Gas Science and Engineering, vol. 40, pp. 141–158, Apr. 2017, doi: [10.1016/j.jngse.2017.02.001](https://doi.org/10.1016/j.jngse.2017.02.001).

[24] M. M.- Fard and F. Pourfayaz, “Advanced exergy analysis of heat exchanger network in a complex natural gas refinery,” *Journal of Cleaner Production*, vol. 206, pp. 670–687, Jan. 2019, doi: [10.1016/j.jclepro.2018.09.166](https://doi.org/10.1016/j.jclepro.2018.09.166)

[25] S. Yuan, “ODE-ORIENTED SEMI-ANALYTICAL METHODS,” in *Computational Mechanics in Structural Engineering*, F. Y. Cheng and Y. Gu, Eds., Oxford: Elsevier Science Ltd, 1999, pp. 375–388. doi: [10.1016/B978-008043008-9/50067-3](https://doi.org/10.1016/B978-008043008-9/50067-3).

[26] T. Berman, A. Lavine, F. Incropera, and D. Dewitt, *Fundamentals of Heat and Mass Transfer*, 7th ed. Wiley, 2011.